Supplementary Information For:

Slow magnetic relaxation in Fe(II) *m*-terphenyl complexes

Andrew J. Valentine,[a] Ana M. Geer,[b] Toby J. Blundell,[a] Will Tovey,[a] Matthew J. Cliffe,[a] E. Stephen Davies,[a] Stephen P. Argent,[a] William Lewis,[d] Jonathan McMaster,[a] Laurence J. Taylor,[a],* Daniel Reta,[e],* and Deborah L. Kays.[a],*

[a] School of Chemistry, University Park, University of Nottingham, Nottingham, NG7 2RD (UK)
[b] Departamento de Química Inorgánica, Instituto de Síntesis Química y Catálisis Homogénea (ISQCH), CSIC Universidad de Zaragoza, Pedro Cerbuna 12, 50009 Zaragoza (Spain)
[c] Department of Chemistry, Durham University, South Road, Durham, DH1 3LE (UK)
[d] School of Chemistry, The University of Sydney, F11, Eastern Ave, Sydney NSW 2006 (Australia)
[e] Kimika Fakultatea, Euskal Herriko Unibertsitatea UPV/EHU & Donostia International Physics Center (DIPC), Euskadi; IKERBASQUE, Basque Foundation for Science, Bilbao (Spain)

* Corresponding Authors

E-mail: laurence.taylor@nottingham.ac.uk; daniel.reta@ehu.eus; deborah.kays@nottingham.ac.uk

Contents

S1 – General Experimental

All air-sensitive manipulations were performed using standard Schlenk line and glovebox techniques under an atmosphere of argon or nitrogen respectively. All solvents were pre-dried, either *via* passage through a drying column of 4 Å molecular sieves (*iso*-hexane, diethyl ether), or *via* distilling over molten potassium (toluene) or sodium/benzophenone (THF). The solvents were stored over a potassium mirror (*iso*-hexane, toluene, diethyl ether) or 4 Å molecular sieves (THF) and degassed *in vacuo* prior to use. Benzene-d_6 was dried over potassium and degassed *via* three freeze-pump-thaw cycles. Organolithium ligand precursors [4-R-2,6-Xyl$_2$C$_6$H$_2$Li]$_2$ (R = *t*Bu, SiMe$_3$, Cl, CF$_3$; where Xyl = 2,6-Me$_2$C$_6$H$_3$) were prepared according to previously published methods.[1] FeCl$_2$·(thf)$_{1.5}$ was obtained by minor modifications of literature methods.[2,3] (2,6-Xyl$_2$C$_6$H$_3$)$_2$Fe (**3**)[4] was prepared using literature methods, and its characterisation matched literature data.[4] All other reagents and solvents were acquired commercially and used as received unless otherwise stated.

S1.1 – Instrumentation

^{1}H and ^{19}F{^{1}H} NMR spectra were recorded using Bruker AV400 or AV(III)400 spectrometers at 25 °C (Figures S2–S7). Chemical shifts are quoted in ppm relative to tetramethylsilane (^{1}H) or CFCl$_3$ (^{19}F{^{1}H}). Mass spectrometry measurements were performed by the National Mass Spectrometry Facility at Swansea University on a Xevo G2-ASAP mass spectrometer with an Atmospheric Solid Analysis Probe (ASAP). Elemental analyses (CHN) were performed by Mr Stephen Boyer of the Microanalysis Service at the London Metropolitan University. IR spectra were recorded as solutions in dry, degassed benzene inside a sealed cell fitted with KBr windows on a Bruker Alpha FTIR instrument in the region of 500–4000 cm^{-1}, then the solvent background was subtracted (Figure S8). UV/Vis samples were prepared in a Young's Tap modified 10 mm quartz cell under dinitrogen in a glovebox. UV/Vis spectra were recorded on a Perkin Elmer Lambda 16 Spectrometer over 290–900 nm (1 nm sampling interval) with background solvent subtraction (Figure S9).

S2 – Synthesis and Characterisation

S2.1 – (4-*t*Bu-2,6-Xyl$_2$C$_6$H$_2$)$_2$Fe (1)

To a mixture of [4-*t*Bu-2,6-Xyl$_2$C$_6$H$_2$Li]$_2$ (500 mg, 0.72 mmol) and FeCl$_2$·(thf)$_{1.5}$ (169 mg, 0.72 mmol), toluene (20 mL) and THF (2 mL) was added, and the resultant green suspension stirred for 16 h at room temperature. Removal of solvent *in vacuo* afforded a yellow-green solid which was dried *in vacuo* at 60 °C for 4 h. The solid was extracted into hexane (2 × 15 mL) and filtered to remove insoluble material. The combined extracts were concentrated *in vacuo* to *ca* 10 mL and stored at −30 °C for 24 h to afford **1** as yellow crystals suitable for X-ray diffraction (308 mg, 58%).

HRMS (ASAP) *m/z* Found: 739.3958; Calc. for C$_{52}$H$_{59}$Fe$^+$ [M+H]$^+$: 739.3967.

Elemental analysis Found: C 84.5, H 8.05; Calc. for C$_{52}$H$_{58}$Fe: C 84.5, H 7.9 %.

^{1}H NMR δ_H (400 MHz, C$_6$D$_6$): 181.6 (4H, s, br, $\Delta\nu_{1/2}$ = 933 Hz, *m*-H C$_6$H$_2$), 52.4 (18H, s, br, $\Delta\nu_{1/2}$ = 99 Hz, *t*Bu), –36.4 (24H, s, br, $\Delta\nu_{1/2}$ = 1186 Hz, Me Xyl), –55.0 (8H, s, br, $\Delta\nu_{1/2}$ = 175 Hz, *m*-H Xyl), –59.5 (4H, s, br, $\Delta\nu_{1/2}$ = 132 Hz, *p*-H Xyl).

UV/Vis (toluene) λ_{max}/nm (ε/mol^{-1} dm^3 cm^{-1}): 363 (1600), 375 (1700), 392 (1100), 427sh (500).

IR ν_{max}(benzene)/cm^{-1} 2918(m), 2898(w), 2865(m), 2734(w), 1579(w), 1435(m), 1378(w), 1362(m), 1260(w), 1238(w), 1104(w), 1086(w); 882(w), 768(w), 577(w), 553(w).

S2.2 – (4-Me$_3$Si-2,6-Xyl$_2$C$_6$H$_2$)$_2$Fe (2)

To a mixture of [4-Me$_3$Si-2,6-Xyl$_2$C$_6$H$_2$Li]$_2$ (500 mg, 0.69 mmol) and FeCl$_2$·(thf)$_{1.5}$ (162 mg, 0.69 mmol), toluene (20 mL) and THF (2 mL) was added, and the resultant green suspension stirred for 16 h at room temperature. Removal of solvent *in vacuo* afforded a yellow-green solid which was dried *in vacuo* at 60 °C for 4 h. The solid was extracted into *iso*-hexane (2 × 15 mL) and filtered to remove insoluble material. The combined extracts were concentrated *in vacuo* to *ca* 10 mL and stored at −30 °C for 24 h to afford **2** as yellow crystals suitable for X-ray diffraction (303 mg, 57%).

HRMS (ASAP) *m/z* Found: 771.3505; Calc. for $C_{50}H_{59}Si_2Fe$ $[M+H]^+$: 771.3505.

Elemental Analysis Found: C 77.7, H 7.8; Calc. for $C_{50}H_{58}Si_2Fe$: C 77.9, H 7.6 %.

^{1}H NMR δ_H (400 MHz, C_6D_6): 181.2 (4H, s, br, $\Delta\nu_{1/2}$ = 1216 Hz, *m*-H C_6H_2), 39.8 (18H, s, br, $\Delta\nu_{1/2}$ = 83 Hz, Me SiMe$_3$), –35.8 (24H, s, br, $\Delta\nu_{1/2}$ = 1567 Hz, Me Xyl), –54.5 (8H, s, br, $\Delta\nu_{1/2}$ = 254 Hz, *m*-H Xyl), –59.0 (4H, s, br, $\Delta\nu_{1/2}$ = 164 Hz, *p*-H Xyl).

UV/Vis (toluene) λ_{max}/nm (ε/mol^{-1} dm^3 cm^{-1}): 361sh (1500), 377 (1400), 395 (960), 427sh (560).

IR ν_{max}(benzene)/cm^{-1} 2918(m), 2897(w), 2861(m), 2844(m), 2793(w), 2734(m), 2358(m), 2344(m), 1435(m), 1378(m), 1359(s), 1263(m), 1245(m), 1128(w), 1084(m), 878(m), 827(m), 807(s), 765(w), 578(w), 569(w), 552(w).

S2.3 – (4-Cl-2,6-Xyl$_2$C$_6$H$_2$)$_2$Fe (4)

To a mixture of [4-Cl-2,6-Xyl$_2$C$_6$H$_2$Li]$_2$ (500 mg, 0.77 mmol) and FeCl$_2$·(thf)$_{1.5}$ (181 mg, 0.77 mmol), toluene (20 mL) and THF (2 mL) was added, and the resultant green suspension stirred for 16 h at room temperature. Removal of solvent *in vacuo* afforded a yellow-green solid which was dried *in vacuo* at 60 °C for 4 h. The solid was extracted into toluene (2 × 15 mL) and filtered to remove insoluble material. The combined extracts were concentrated *in vacuo* to *ca* 10 mL and stored at −30 °C for 24 h to afford **4** as yellow-green crystals suitable for X-ray diffraction (229 mg, 43%).

HRMS (ASAP) *m/z* Found: 693.1979; Calc. for $C_{45}H_{40}Cl_2FeH^+$ $[M+H]^+$: 693.1981.

Elemental analysis Found: C 75.8, H 5.9; Calc. for $C_{44}H_{40}Cl_2Fe$: C 76.0; H, 5.8%.

^{1}H NMR δ_H (400 MHz, C_6D_6): 176.8 (4H, s, br, $\Delta\nu_{1/2}$ = 1317 Hz, *m*-H C_6H_2), –34.2 (24H, s, br, $\Delta\nu_{1/2}$ = 1769 Hz, Me Xyl), –54.1 (8H, s, br, $\Delta\nu_{1/2}$ = 289 Hz, *m*-H Xyl), –59.1 (4H, s, br, $\Delta\nu_{1/2}$ = 199 Hz, *p*-H Xyl).

UV/Vis (toluene) λ_{max}/nm (ε/mol^{-1} dm^3 cm^{-1}): 365 (1500), 377 (1600), 396 (1200).

IR ν_{max}(benzene)/cm^{-1} 2919(m), 2898(w), 2860(m), 2846(m), 2736(m), 2357(w), 2345(w), 1735(w), 1555(s), 1435(s), 1377(m), 1289(s), 1107(m), 1084(m), 874(w), 820(s), 768(w), 580(w), 550(w).

S2.4 – (4-F$_3$C-2,6-Xyl$_2$C$_6$H$_2$)$_2$Fe (5)

To a mixture of [4-F$_3$C-2,6-Xyl$_2$C$_6$H$_2$Li]$_2$ (300 mg, 0.42 mmol) and FeCl$_2$·(thf)$_{1.5}$ (98 mg, 0.42 mmol), diethyl ether (20 mL) was added, and the resultant yellow-green suspension stirred for 16 h at room temperature. Removal of solvent *in vacuo* afforded a yellow-green solid which was dried *in vacuo* at room temperature for 4 h. The solid was extracted into *iso*-hexane (2 × 15 mL) and filtered to remove

insoluble material. The combined extracts were concentrated *in vacuo* to *ca* 7 mL and stored at −30 °C for 24 h to afford **5**·$(C_6H_{14})_{0.5}$ as yellow crystals suitable for X-ray diffraction (141 mg, 42%). N.B. Satisfactory CHN analysis could not be obtained for this compound; this is attributed to its very high air sensitivity, the presence of C–F bonds, and the presence of co-crystallised solvent.

HRMS (ASAP) *m/z* Found: 762.2377; Calc. for $C_{46}H_{40}F_6Fe^+$ $[M]^+$: 762.2385.

^{1}H NMR δ_H (400 MHz, C_6D_6): 174.5 (4H, s, br, $\Delta\nu_{1/2}$ = 805 Hz, *m*-H C_6H_2), –33.2 (24H, s, br, $\Delta\nu_{1/2}$ = 1008 Hz, Me Xyl), –53.2 (8H, s, br, $\Delta\nu_{1/2}$ = 204 Hz, *m*-H Xyl), –58.3 (4H, s, br, $\Delta\nu_{1/2}$ = 151 Hz, *p*-H Xyl).

^{19}F{^{1}H} NMR δ_F (376 MHz, C_6D_6): –62.0 (s).

UV/Vis (toluene) λ_{max}/nm (ε/mol^{-1} dm^3 cm^{-1}): 369sh (830), 387 (650), 410sh (500)

IR ν_{max}(benzene)/cm^{-1} 2919(w), 2897(w), 2866(w), 2845(w), 2736(w), 1431(w), 1378(w), 1343(s), 1263(m), 1241(w), 1121(m), 1104(w), 893(w).

S3 – Supplementary Spectroscopic Data

S3.1 – NMR Spectra

Table S1: Experimental chemical shifts (ppm) of resonances corresponding to the *meta*-hydrogen of the central aryl ring (*m*-H C_6H_2) and the methyl groups of the flanking 2,6-Xyl aryl rings (Me Xyl) in the paramagnetic ^{1}H NMR spectra of **1**–**5**.

Compound	R	*m*-H C_6H_2 (ppm)	Me Xyl (ppm)
1	*t*Bu	181.6	−36.4
2	$SiMe_3$	181.2	−35.8
3	H	178.9	−35.3
4	Cl	176.8	−34.2
5	CF_3	174.5	−33.2

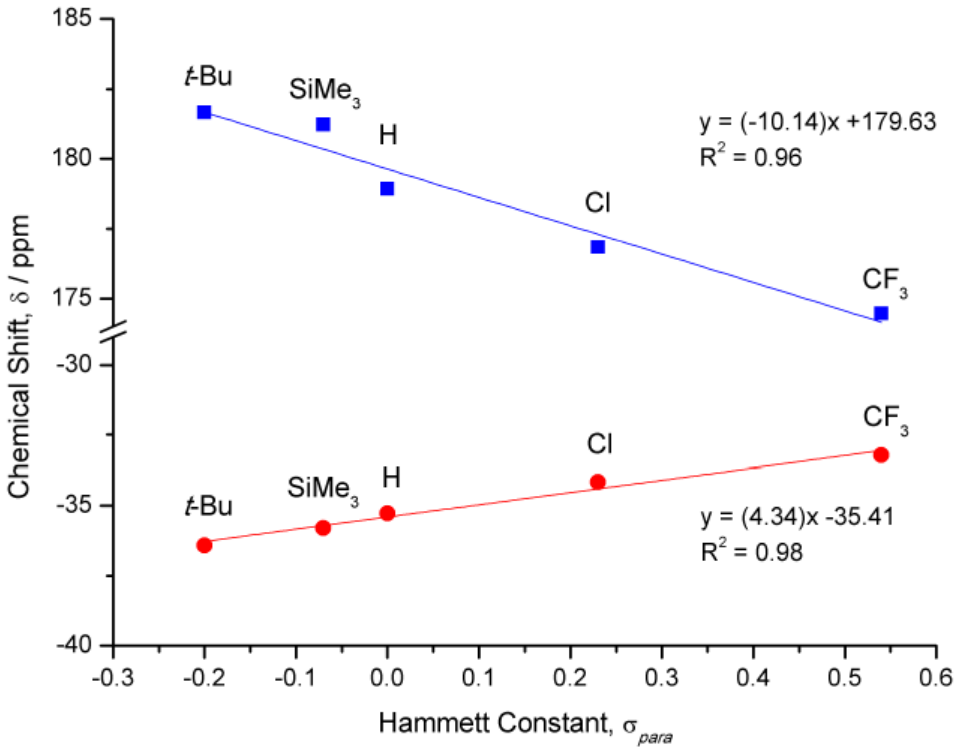

Figure S1: Plot of the ^{1}H NMR chemical shift (δ) for the C_6H_2 *m*-H signals (blue squares) and Xyl Me signals (red circles) of complexes **1**–**5** versus the Hammett Constant (σ_{para})[5] of the ligand R group (*t*Bu, $SiMe_3$, H, Cl, CF_3). Lines represent linear fits of the data.

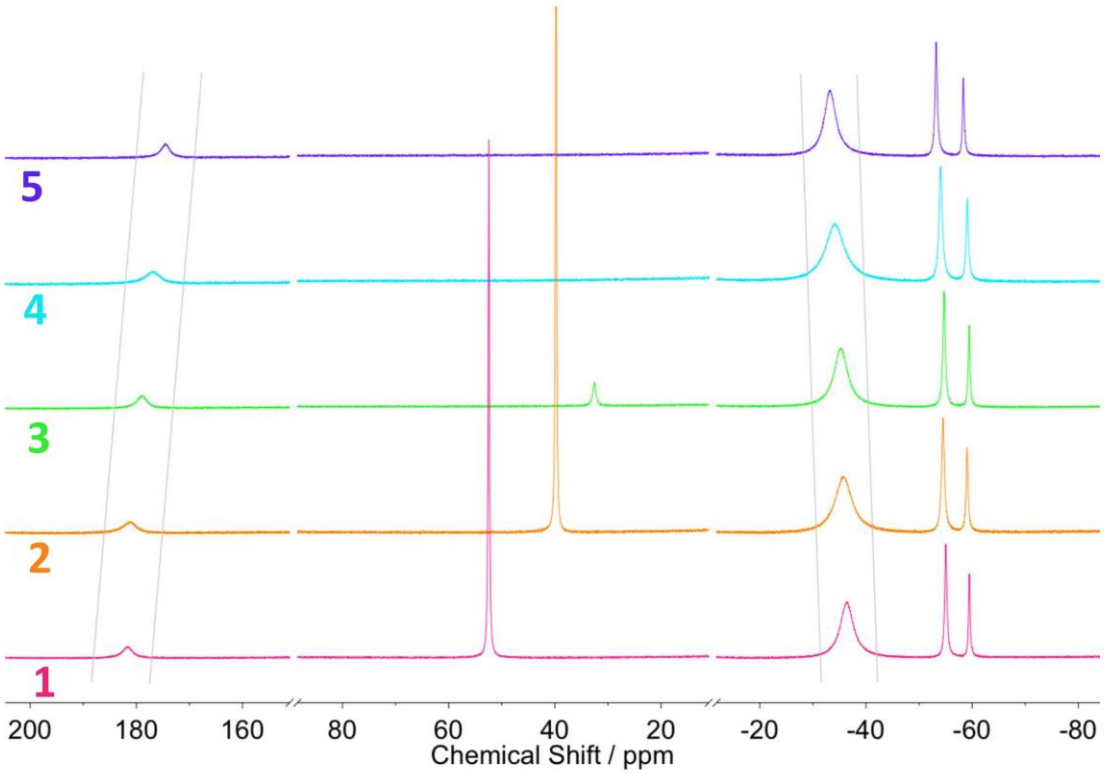

Figure S2: Stacked ^{1}H NMR spectra for complexes **1**–**5** with resonances for *m*-H of central aryl ring (*ca* 180 ppm) and methyl groups of xylyl rings (*ca* −35 ppm) highlighted.

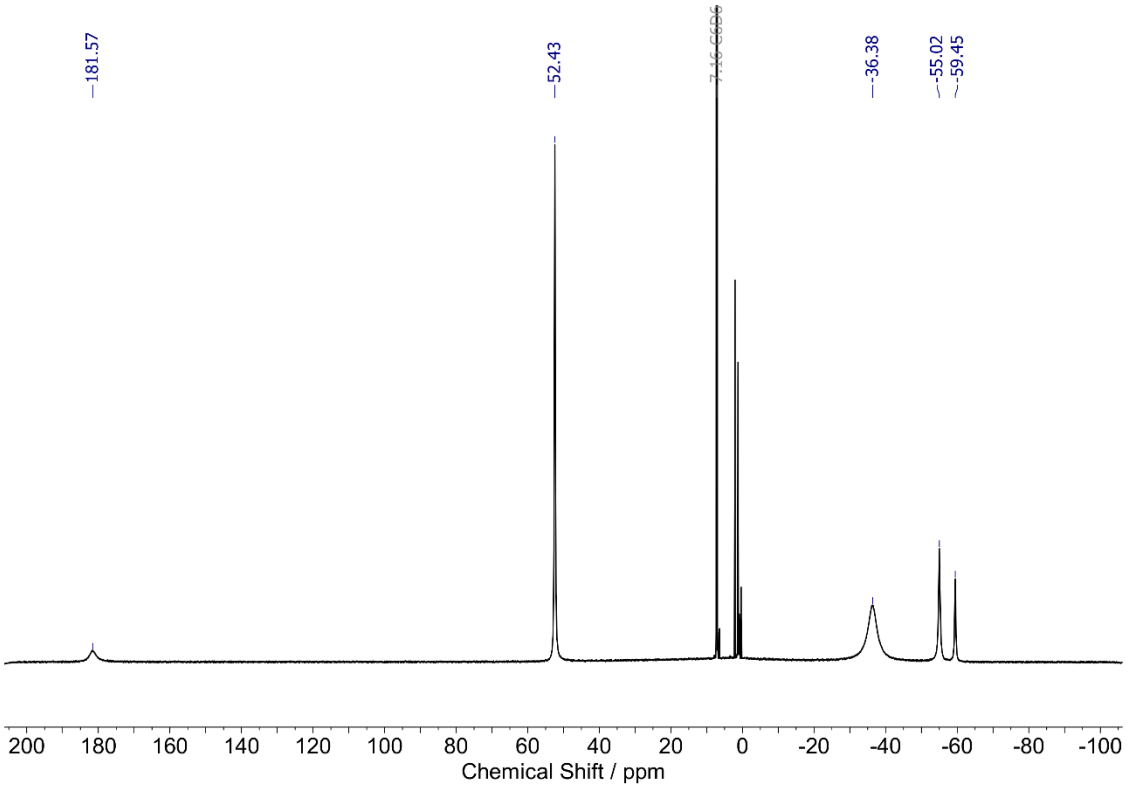

Figure S3: ^{1}H NMR spectrum of (4-*t*Bu-2,6-Xyl$_2$C$_6$H$_3$)$_2$Fe (**1**) recorded at 400 MHz (C$_6$D$_6$, 25 °C).

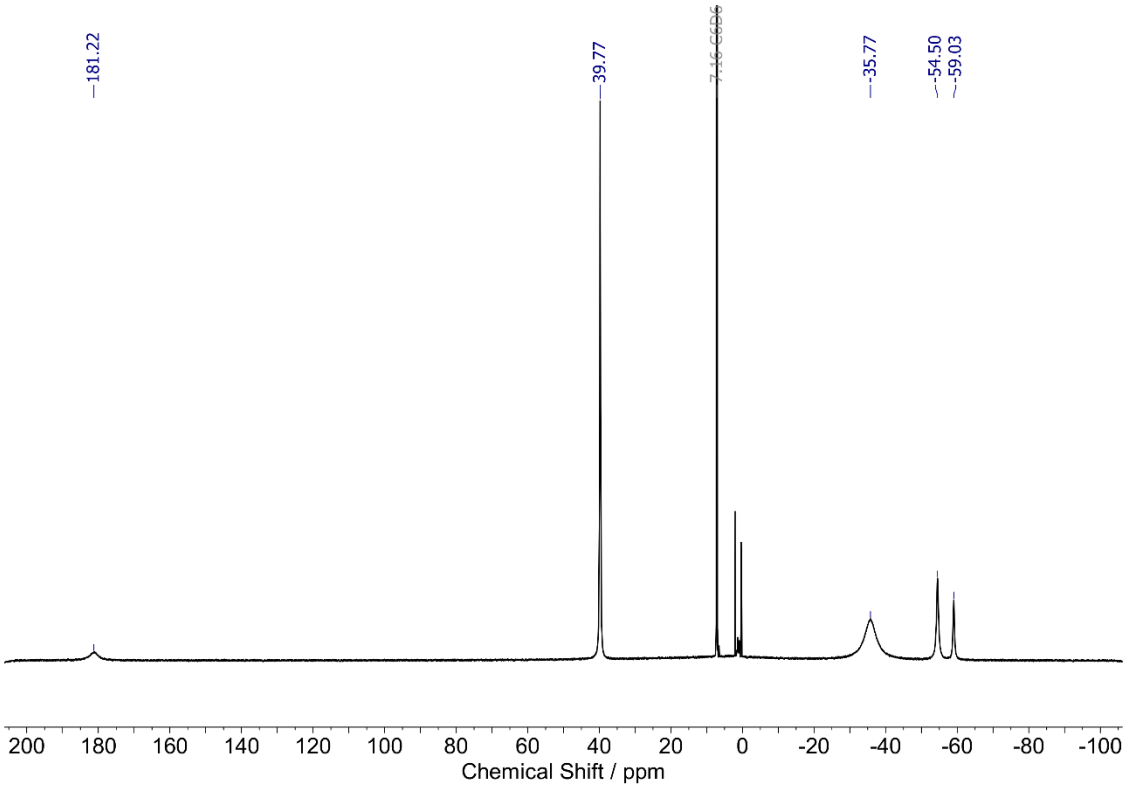

Figure S4: ^{1}H NMR spectrum of (4-Me$_3$Si-2,6-Xyl$_2$C$_6$H$_3$)$_2$Fe (**2**) recorded at 400 MHz (C$_6$D$_6$, 25 °C).

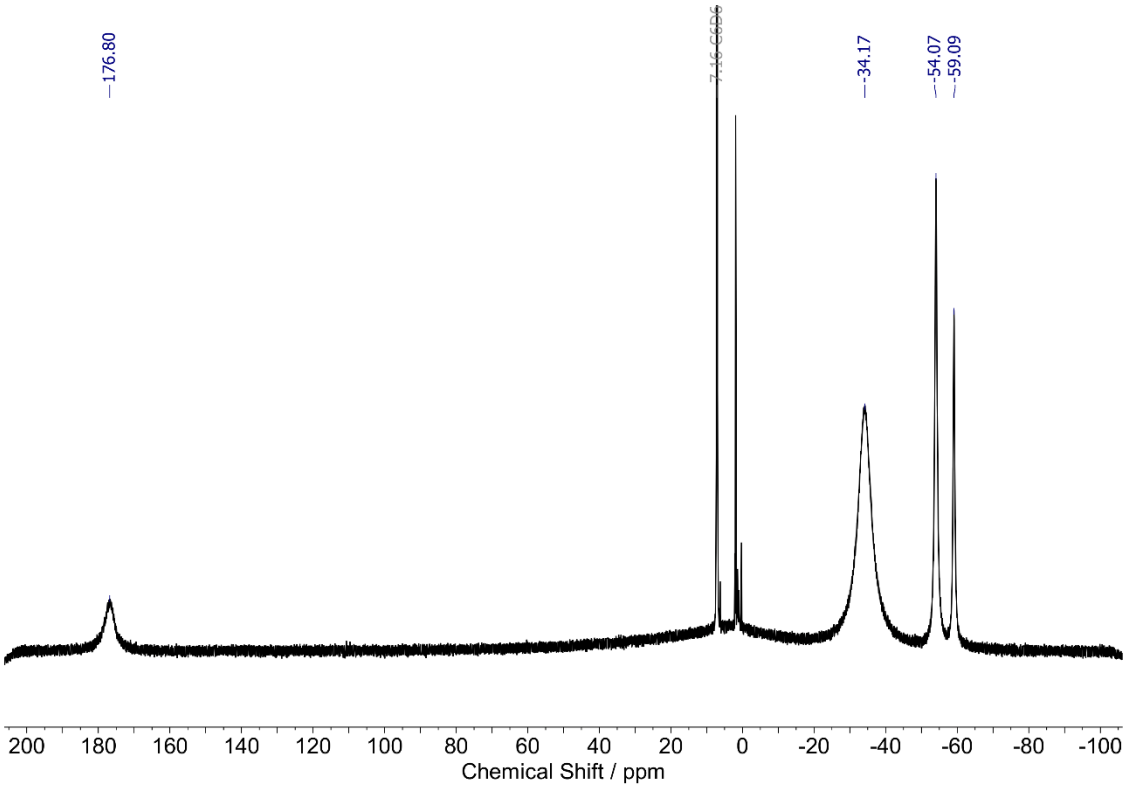

Figure S5: ^{1}H NMR spectrum of (4-Cl-2,6-Xyl$_2$C$_6$H$_3$)$_2$Fe (**4**) recorded at 400 MHz (C$_6$D$_6$, 25 °C).

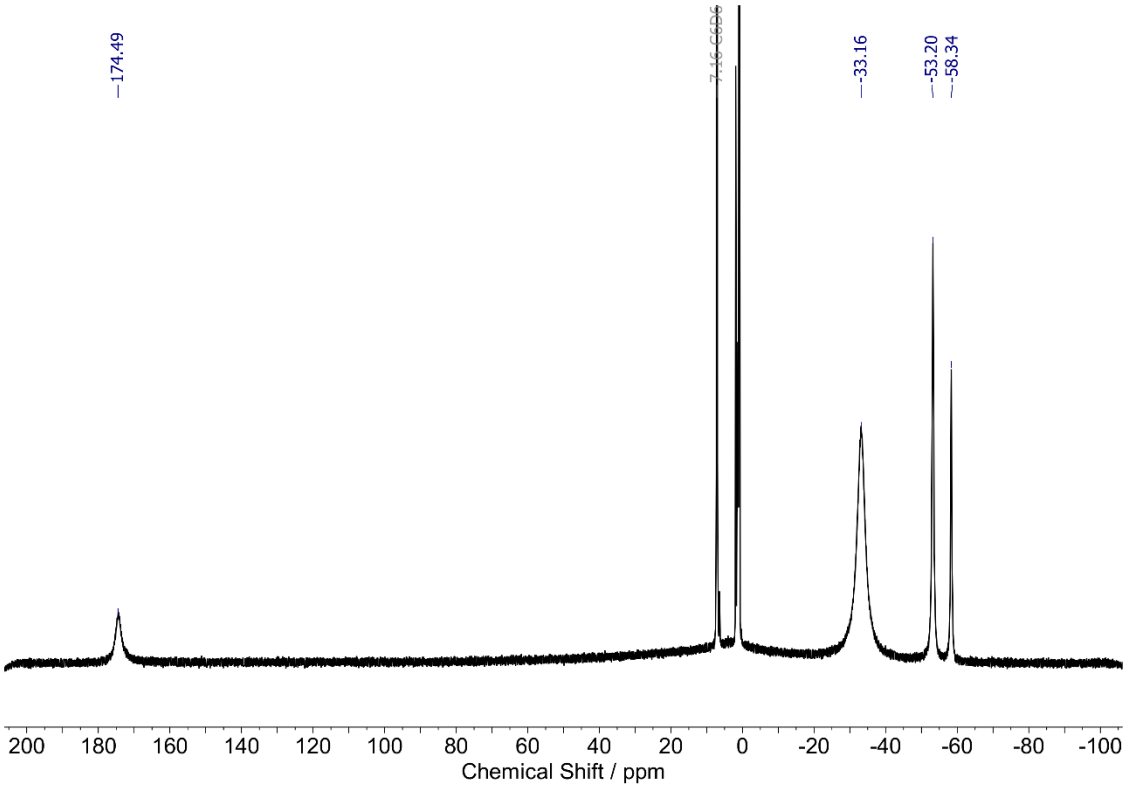

Figure S6: ^{1}H NMR spectrum of (4-F$_3$C-2,6-Xyl$_2$C$_6$H$_3$)$_2$Fe (**5**) recorded at 400 MHz (C$_6$D$_6$, 25 °C).

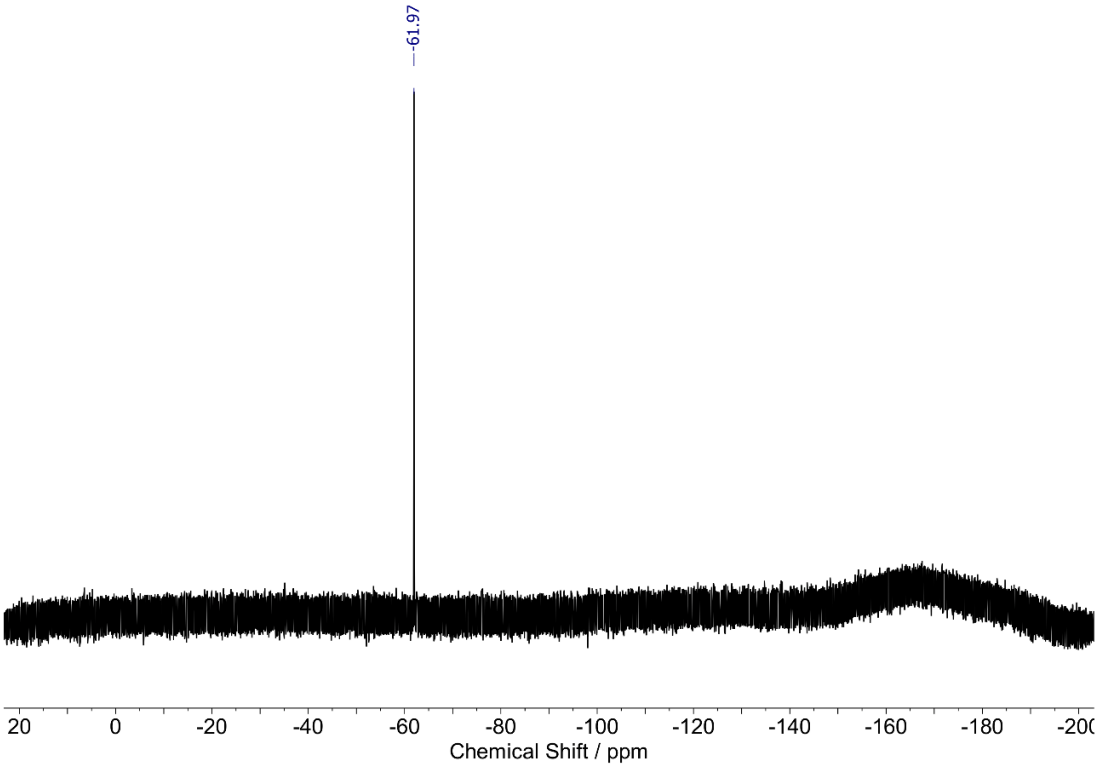

Figure S7: $^{19}F\{^{1}H\}$ NMR spectrum of (4-F_3C-2,6-$Xyl_2C_6H_3$)$_2$Fe (**5**) recorded at 376 MHz (C_6D_6, 25 °C).

S3.2 – IR Spectra

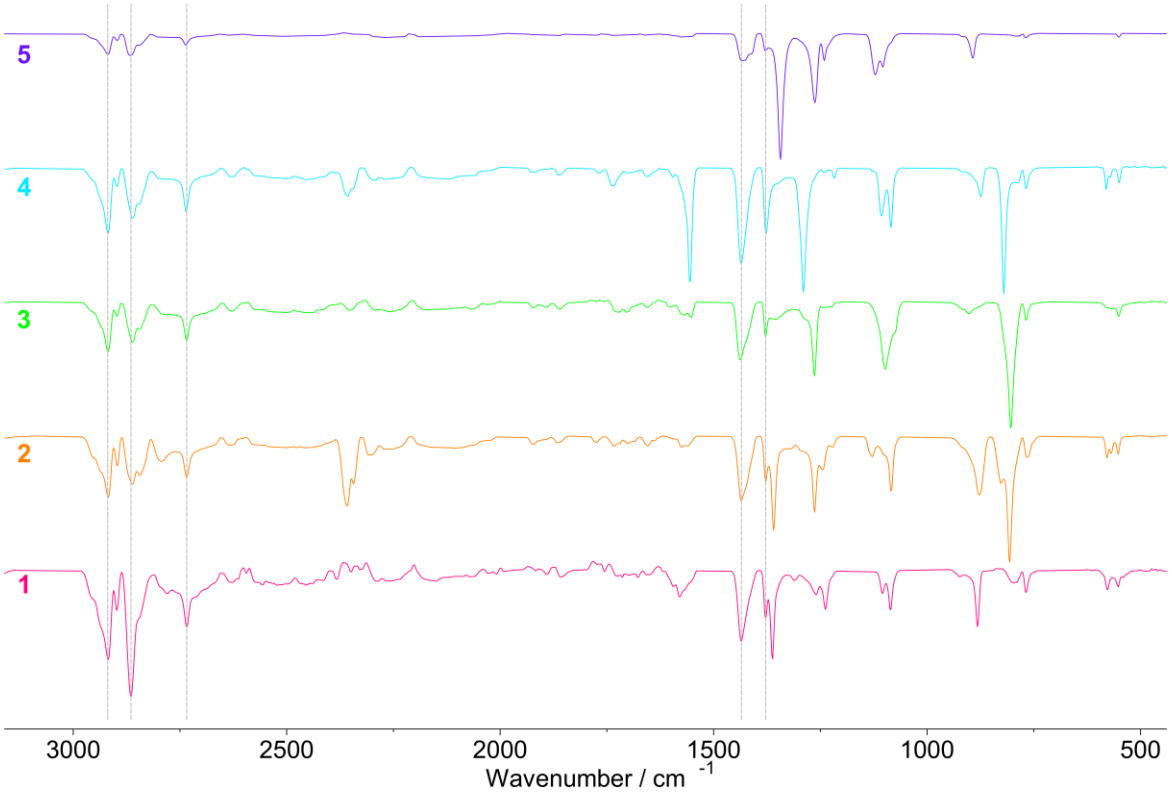

Figure S8: IR spectra of complexes **1–5** collected in C_6H_6 with background solvent subtraction.

S3.3 – UV/Vis Spectra

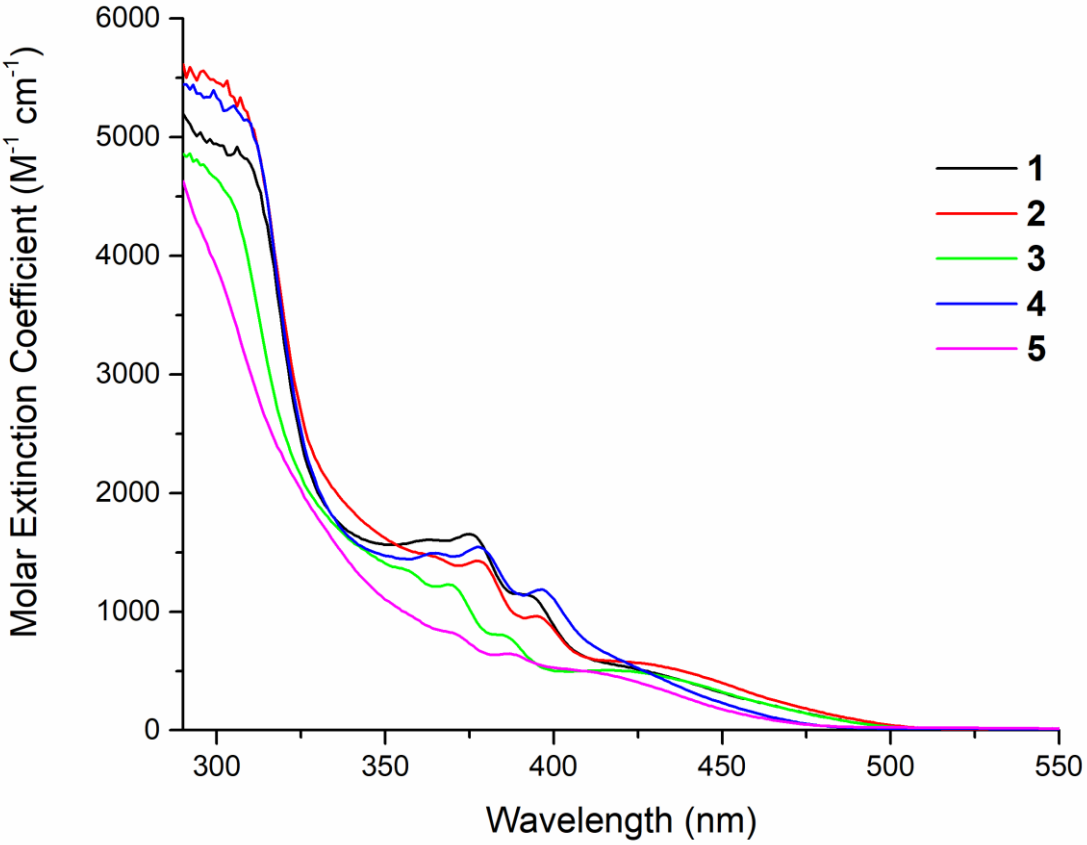

Figure S9: UV/Visible absorption spectra of **1**–**5** showing Molar Extinction Coefficient (M^{-1} cm^{-1}) versus wavelength (nm). All spectra recorded as 0.6 mM solutions in toluene with background solvent subtraction. No significant absorption was observed for **1**–**5** at wavelengths > 550 nm.

S4 – Single Crystal X-ray Diffraction

S4.1 – Methodology

Suitable single crystals of (4-R-2,6-$Xyl_2C_6H_3)_2Fe$ [R = *t*Bu (**1**), $SiMe_3$ (**2**), H (**3**), Cl (**4**), CF_3 (**5**)] were selected under the protection of Fomblin® (YR-1800 perfluoropolyether oil) then mounted on a polymer-tipped MicroMount™ and rapidly cooled with a stream of N_2 at 120 K. The data were collected on either an Oxford Diffraction GV1000 (TitanS2 CCD area detector, mirror-monochromated Cu-Kα radiation source; λ = 1.54184 Å, ω scans) or an Oxford Diffraction GV1000 (AtlasS2 CCD area detector, mirror-monochromated Cu-Kα radiation source; λ = 1.54184 Å, ω scans) or an XtaLAB PRO MM007 (PILATUS3 R 200K Hybrid Pixel Array detector, mirror-monochromated Cu-Kα radiation source; λ = 1.54184 Å, ω scans). Cell parameters were refined in each data set from the observed positions of all strong reflections, and Gaussian based absorption corrections with a beam profile correction (CrysAlisPro) were applied.[6] The crystal structures were solved using ShelXT[7] with intrinsic phasing methods and refined by ShelXL with least-squares procedures[8] using the Olex2 software package for molecular graphics.[9] All non-H atoms were refined anisotropically. All H atoms were

placed at calculated position and refined by using a geometric riding model. The crystal for complex **1** was a weakly diffracting non-merohedral twin with a diffraction limit of 0.95 Å, hence, the data used for the refinement was truncated to this resolution. The structure for **1** was solved and refined against the hklf4 file, refinement against the hklf5 resulted in an increased R_1 and wR_2. Complex **5** contained disordered solvent (*iso*-hexane, 0.5 molecules per formula unit) which could not be modelled sensibly and was excluded from the electron density map using the solvent mask implemented in Olex2.[9]

CCDC 2184650-2184653 contain the supplementary crystallographic data for this article. These data can be obtained free of charge from The Cambridge Crystallographic Data Centre *via* www.ccdc.cam.ac.uk/structures.

S4.2 – Supplementary Crystal Data

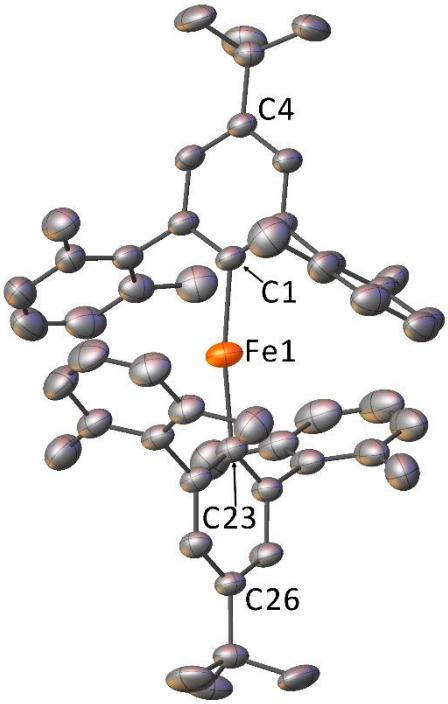

Figure S10: Crystal structure of **1** with displacement ellipsoids set to 30%. Hydrogen atoms and minor disorder components omitted for clarity.

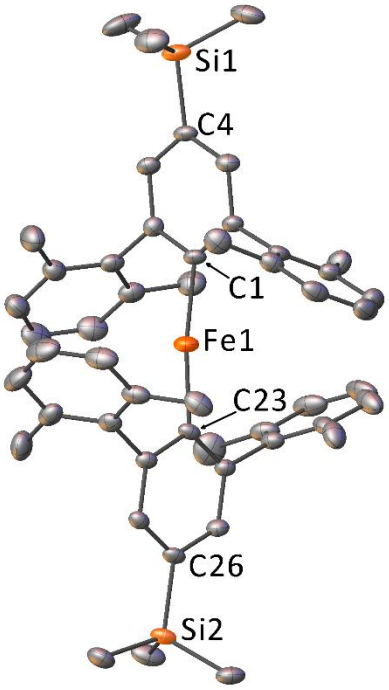

Figure S11: Crystal structure of **2** with displacement ellipsoids set to 50%. Hydrogen atoms and additional 0.5 molecules in the asymmetric unit omitted for clarity.

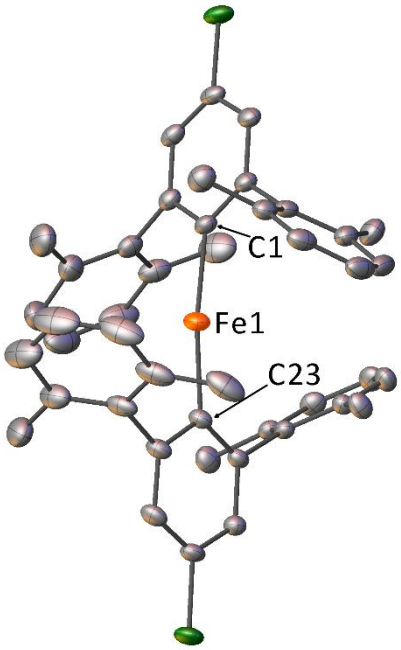

Figure S12: Crystal structure of **4** with displacement ellipsoids set to 50%. Hydrogen atoms and additional 2 molecules in the asymmetric unit omitted for clarity.

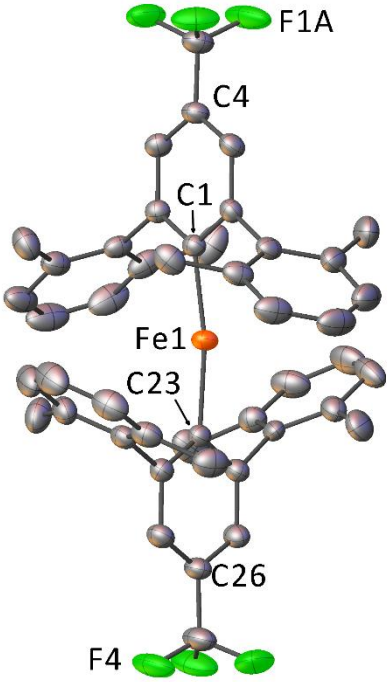

Figure S13: Crystal structure of **5** with displacement ellipsoids set to 50%. Hydrogen atoms, minor disorder component, and co-crystallised *iso*-hexane omitted for clarity.

Table S2: Summary of crystallographic data for **1**–**5**. [a]Data for complex **3** taken from the literature[4] and presented here for ease of comparison.

	1	**2**	**3**[a]	**4**	**5**
Empirical formula	$C_{52}H_{58}Fe$	$C_{50}H_{58}FeSi_2$	$C_{44}H_{42}Fe$	$C_{44}H_{40}Cl_2Fe$	$C_{49}F_6FeH_{47}$
Formula weight	738.83	770.99	626.62	695.51	805.71
Temperature/K	120(2)	120(2)	120(2)	120(2)	120(2)
Crystal system	monoclinic	monoclinic	tetragonal	monoclinic	monoclinic
Space group	$P2_1/c$	$C2/c$	$P4_3$	$P2_1/c$	$P2_1/c$
a/Å	12.9745(14)	25.4389(10)	10.48569(11)	22.1189(2)	11.31550(10)
b/Å	16.9307(18)	11.5117(4)	-	19.6861(2)	17.9907(2)
c/Å	20.1943(15)	47.1469(18)	30.7962(6)	24.7347(2)	20.6727(2)
α/°	90	90	90	90	90
β/°	96.822(8)	102.414(4)	90	95.9930(10)	98.4560(10)
γ/°	90	90	90	90	90
Volume/Å^3	4404.6(7)	13483.9(9)	3386.03(9)	10711.49(17)	4162.67(7)
Z	4	12	4	12	4
ρ_{calc} g/cm^3	1.114	1.139	1.229	1.294	1.286
μ/mm^{-1}	2.971	3.424	3.778	4.981	3.404
F(000)	1584	4944	-	4368	1684
Crystal size/mm^3	0.258 × 0.218 × 0.054	0.444 × 0.136 × 0.068	-	0.55 × 0.487 × 0.309	0.567 × 0.363 × 0.325
Radiation	Cu $K\alpha$ (λ = 1.54184)	Cu $K\alpha$ (λ = 1.54184)	Cu $K\alpha$ (λ = 1.54184)	Cu $K\alpha$ (λ = 1.54184)	Cu $K\alpha$ (λ = 1.54184)
2Θ range for data collection/°	6.834 to 109.052	7.116 to 149.312	8.432 to 148.558	6.798 to 147.918	6.544 to 146.138
Reflections collected	20637	79133	21453	92429	76387
Independent reflections	5295 [R_{int} = 0.0949, R_{sigma} = 0.0785]	13471 [R_{int} = 0.1280, R_{sigma} = 0.0721]	6709 [R_{int} = 0.0422, R_{sigma} = 0.0341]	21283 [R_{int} = 0.0554, R_{sigma} = 0.0305]	8270 [R_{int} = 0.0331, R_{sigma} = 0.0146]
Goodness-of-fit on F^2	0.943	1.062	-	1.055	1.051
Final R indexes [I>=2σ (I)]	R_1 = 0.0551, wR_2 = 0.1296	R_1 = 0.0844, wR_2 = 0.1951	-	R_1 = 0.0522, wR_2 = 0.1509	R_1 = 0.0350, wR_2 = 0.0968
Final R indexes [all data]	R_1 = 0.1147, wR_2 = 0.1494	R_1 = 0.1103, wR_2 = 0.2115	R_1 = 0.0308, wR_2 = 0.0794	R_1 = 0.0558, wR_2 = 0.1558	R_1 = 0.0365, wR_2 = 0.0983
Largest diff. peak/hole / e Å^{-3}	0.24/–0.29	0.77/–0.75	-	1.15/–0.72	0.31/–0.41

S5 – Cyclic Voltammetry

S5.1 – Methodology

Samples for cyclic voltametric studies were prepared within the glovebox under dinitrogen as 1 mM solutions of **1**–**5** in THF containing 0.5 M [*n*Bu$_4$N][BF$_4$] electrolyte. The solutions were sealed inside a single-compartment electrochemical cell that functioned as a three-electrode system comprising of glassy carbon working and counter electrodes, and a saturated calomel reference electrode (SCE) that was chemically isolated from the sample solution via a bridge tube containing electrolyte solution and terminated with a porous ceramic frit. Cyclic voltametric experiments were carried out under nitrogen on an Autolab PGSTAT320N potentiostat and redox potentials are referenced to the ferrocenium-ferrocene (Fc^+/Fc) couple by an internal calibration.

Cyclic voltammograms for **1**–**5** at various scan rates are shown in Figures S15–S19. Experimental values of cathodic peak potential ($E_{p,c}$), anodic peak potential ($E_{p,a}$), mid-potential ($E_{1/2}$), cathodic peak current ($I_{p,c}$), anodic peak current ($I_{p,a}$) and peak current ratio ($|I_{p,a}/I_{p,c}|$) at various scan rates are presented in Table S3. Plots showing a linear correlation between $I_{p,c}$ and the square root of the scan rate ($\upsilon^{1/2}$) are presented in Figure S20.

S5.2 – Supplementary Electrochemistry Data

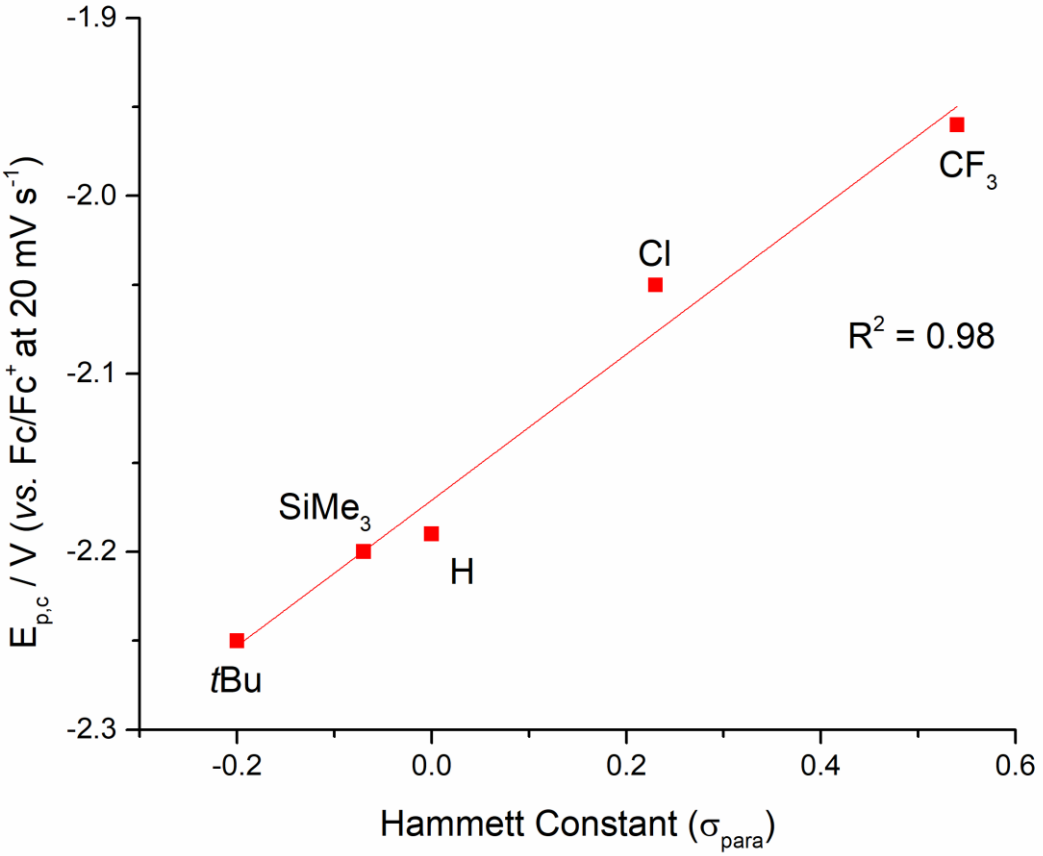

Figure S14: Plot of the cathodic reduction potentials ($E_{p,c}$) recorded at 20 mV/s for **1**–**5** as a function of the Hammett constant (σ_{para})[5] of their R substituent (*t*Bu, SiMe$_3$, H, Cl, CF$_3$). Red line represents a linear fit of the data.

Table S3: Cyclic voltammetric data for (4-R-2,6-Xyl$_2$C$_6$H$_3$)$_2$Fe [R = *t*Bu (**1**), SiMe$_3$ (**2**), H (**3**), Cl (**4**), CF$_3$ (**5**)]. A lack of entry indicates that a peak was not resolved under those conditions.

Compound	υ (mV/s)	$E_{p,c}$ (V)	$E_{p,a}$ (V)	$E_{1/2}$ (V)	$I_{p,c}$ (μA)	$I_{p,a}$ (μA)	$\lvert I_{p,a}/I_{p,c} \rvert$
1	20	-2.25	-	-	-6.33	-	-
	50	-2.27	-	-	-9.59	-	-
	100	-2.28	-2.18	-2.23	-12.14	3.91	0.32
	200	-2.29	-2.18	-2.24	-16.30	6.55	0.40
	300	-2.30	-2.17	-2.24	-19.29	8.29	0.43
	500	-2.30	-2.17	-2.24	-23.77	11.13	0.47
2	20	-2.20	-2.12	-2.16	-5.89	4.16	0.71
	50	-2.21	-2.12	-2.17	-8.98	6.92	0.77
	100	-2.22	-2.11	-2.17	-12.77	9.51	0.74
	200	-2.23	-2.10	-2.17	-16.69	13.85	0.83
	300	-2.23	-2.10	-2.17	-19.84	16.74	0.84
3	20	-2.19	-	-	-8.15	-	-
	50	-2.21	-	-	-12.70	-	-
	100	-2.22	-	-	-17.32	-	-
	200	-2.24	-2.11	-2.18	-23.19	5.91	0.25
	300	-2.24	-2.11	-2.18	-27.23	8.26	0.30
	500	-2.26	-2.11	-2.19	-33.48	12.97	0.39
4	20	-2.05	-1.96	-2.01	-5.30	3.74	0.71
	50	-2.06	-1.96	-2.01	-8.07	6.17	0.76
	100	-2.07	-1.95	-2.01	-11.37	8.20	0.72
	200	-2.08	-1.94	-2.01	-15.03	11.42	0.76
	300	-2.09	-1.93	-2.01	-17.84	13.25	0.74
	500	-2.10	-1.92	-2.01	-21.61	15.64	0.72
5	20	-1.96	-	-	-5.76	-	-
	50	-1.98	-	-	-8.81	-	-
	100	-2.01	-	-	-11.76	-	-
	200	-2.01	-1.86	-1.94	-15.93	4.13	0.26
	300	-2.02	-1.86	-1.94	-18.79	6.32	0.34
	500	-2.04	-1.84	-1.94	-22.78	8.76	0.38

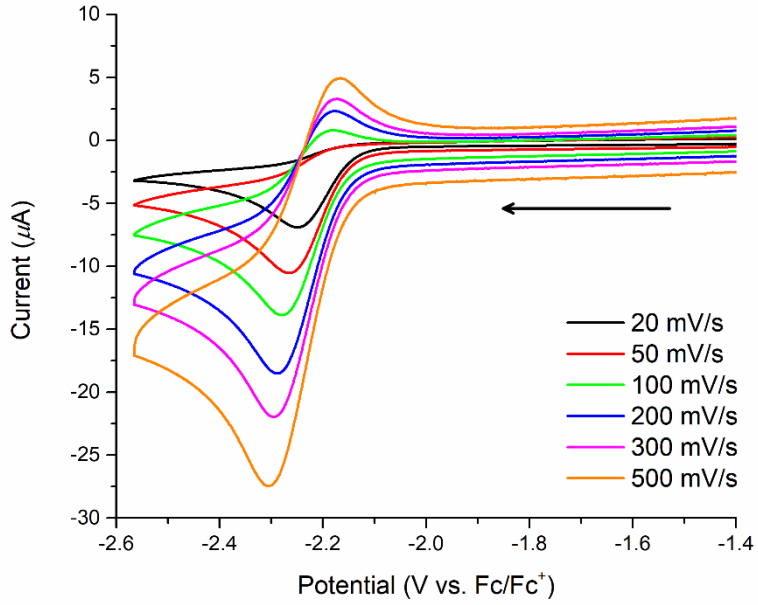

Figure S15: Cyclic voltammograms for **1** (R = *t*Bu) recorded at scan rates from 20–500 mV/s.

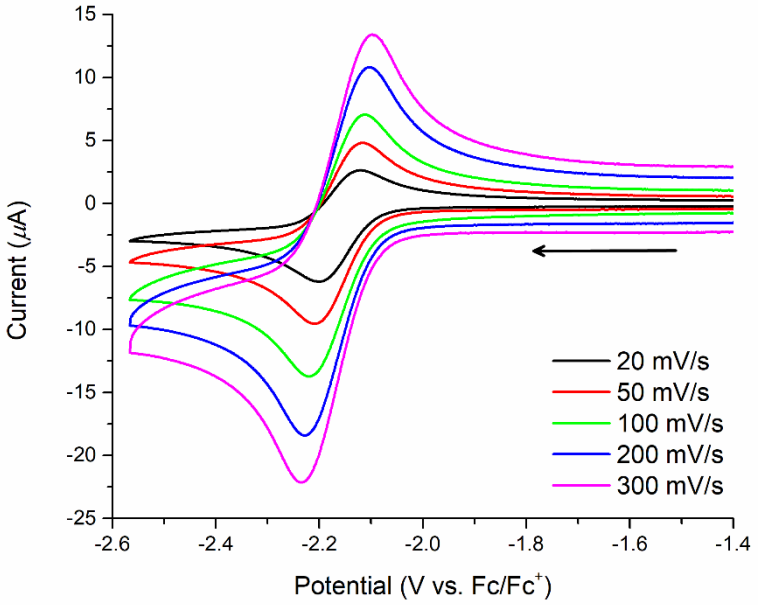

Figure S16: Cyclic voltammograms for **2** (R = $SiMe_3$) recorded at scan rates from 20–300 mV/s.

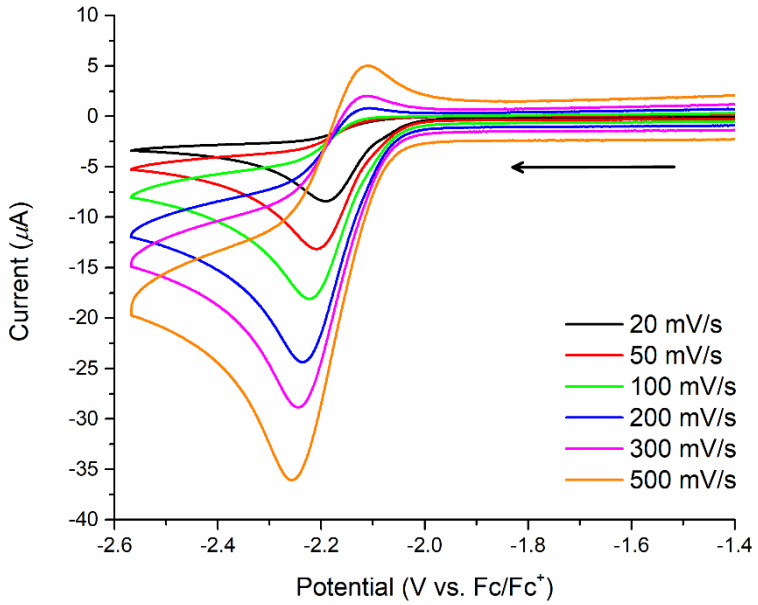

Figure S17: Cyclic voltammograms **3** (R = H) recorded at scan rates from 20–500 mV/s.

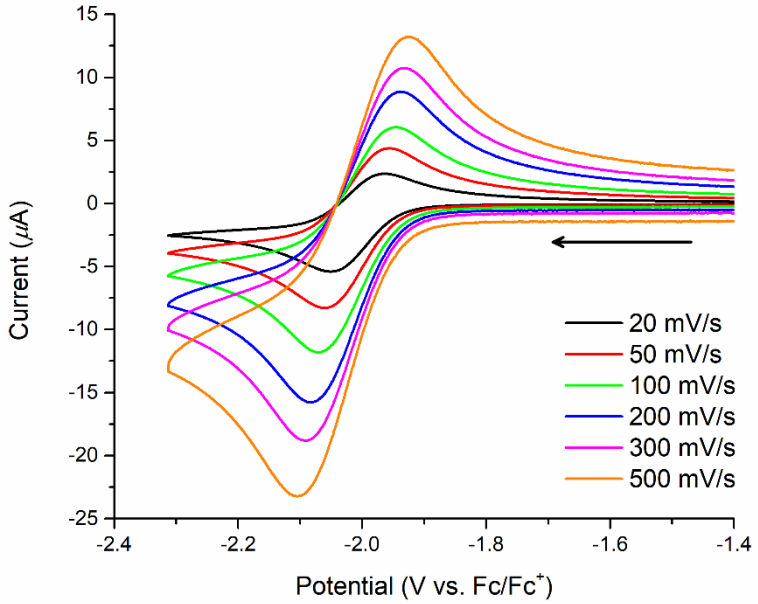

Figure S18: Cyclic voltammograms for **4** (R = Cl) recorded at scan rates from 20–500 mV/s.

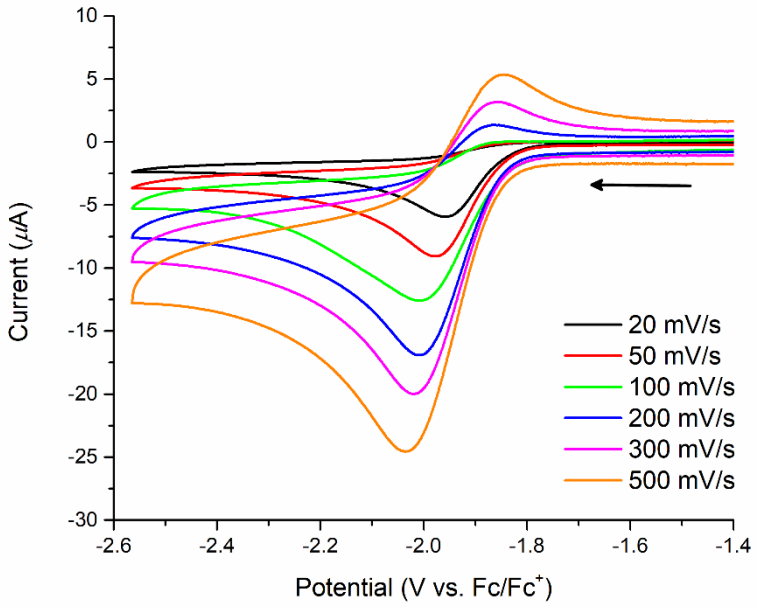

Figure S19: Cyclic voltammograms for **5** (R = CF_3) recorded at scan rates from 20–500 mV/s.

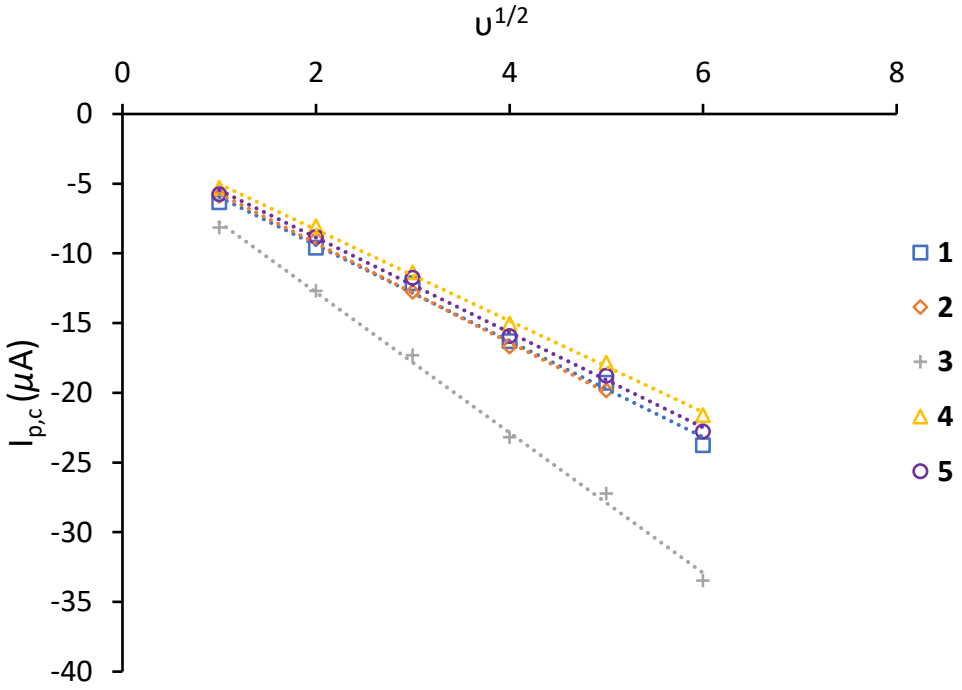

Figure S20: Plot of cathodic peak current ($I_{p,c}$) versus the square-root of the scan rate ($\upsilon^{1/2}$, υ = mV s^{-1}) for **1**–**5**.

S6 – Electronic Structure Calculations

S6.1 – Methodology

The electronic structures of all compounds were studied using OpenMolcas[15] to perform CASSCF-SO calculations. Molecular geometries were taken from the single crystal XRD structure with no optimization, taking the largest disorder component only. For those crystals presenting more than one unique molecule in the unit cell (**2**, **4**), calculations were performed in all of them (indicated as $\mathbf{2_1}$, $\mathbf{2_2}$ for **2**; $\mathbf{4_1}$, $\mathbf{4_2}$, $\mathbf{4_3}$ for **4**). Basis sets from ANO-RCC library[16,17] were employed with VQZP quality for Co and Fe atoms, VTZP quality for the two coordinating carbon atoms, VDZ quality for hydrogen atoms and VDZP for all remaining atoms, employing the second-order DKH transformation. Cholesky decomposition of the two-electron integrals with a threshold of 10^{-8} was performed to save disk space and reduce computational demand. The molecular orbitals (MOs) were optimized in state-averaged CASSCF calculations within each spin manifold, which were then mixed by spin orbit coupling using the RASSI module (see Table S4 for details). The resulting spin-orbit wavefunctions were then used to calculate the magnetic susceptibility and magnetisation curves under a zero external magnetic field using SINGLE_ANISO.[18]

Multistate CASPT2[19] calculations were also performed to address whether dynamical correlation effects could account for deviations from experiment; we focus on **1** as it presents the largest disagreement. Using the state averaged (5 roots) CAS(6,5)SCF wavefunction of the ground spin quintet as zero-order, CASPT2 corrections were calculated also for the five S=2 roots. Mirroring the approach employed for the CASSCF calculations, after convergence of the CASPT2 calculation, RASSI was employed to mix the resulting wavefunctions and SINGLE_ANISO was employed to parametrise the zero-field splitting parameters. The thus-obtained results are displayed alongside the CASSCF results for **1** in Table S8. Given that CASPT2 yields a quantitatively comparable picture as to CASSCF for **1**, it was not applied to the rest of the compounds.

Table S4: Computational approach employed to describe complexes **1**–**5**.

CAS(e,o)SCF	Spin multiplicity	CASSCF / RASSI roots	CASPT2 / RASSI roots
e = 6 o = 5	5	5 / 5	5 / 5
	3	45 / 45	
	1	50 / 50	

S6.2 – Magnetic Susceptibility Simulations

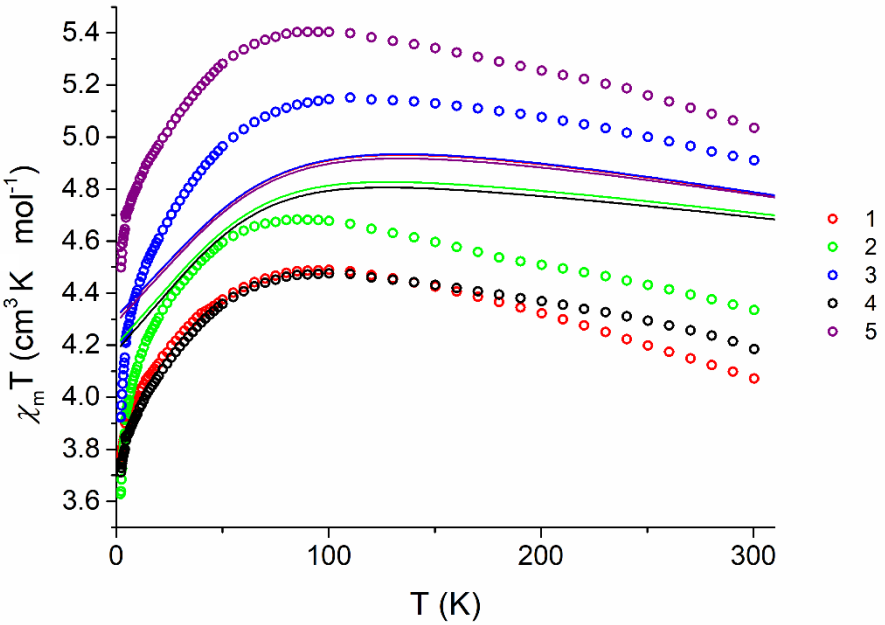

Figure S21: Comparison of experimental (circles) and simulated (CASSCF-SO, solid lines) temperature dependence of $\chi_m T$ for **1**–**5**.

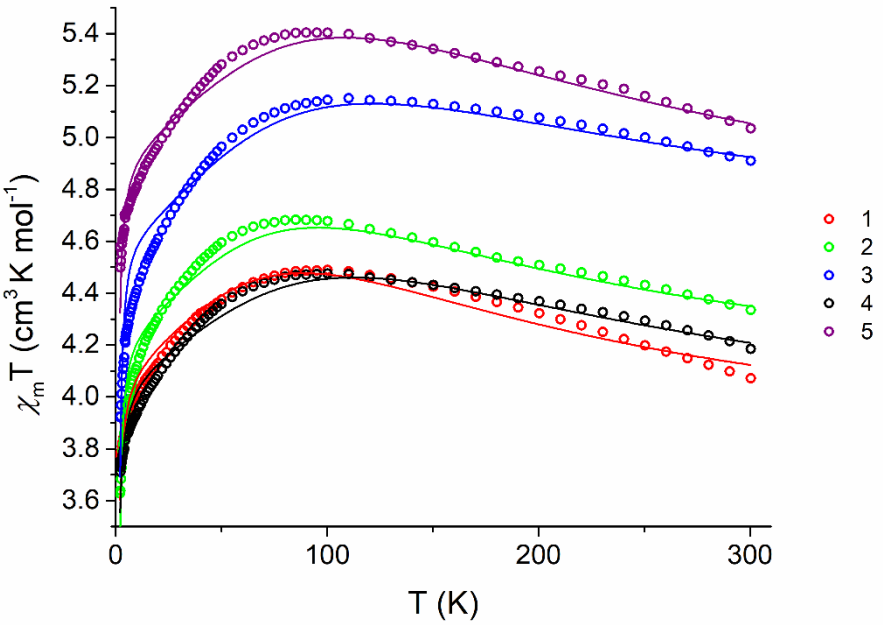

Figure S22: Comparison of experimental (circles) and and fitted (*fit1*, solid lines)[12] temperature dependence of $\chi_m T$ for **1**–**5**.

S6.3 – Supplementary Data Tables

Table S5: Energies (cm^{-1}) of spin-only and spin-orbit coupled states for **1**–**5** calculated with the approach detailed in Table S4. Light, medium, and dark grey refer to quintet, triplet and singlet spin multiplicities, respectively. For spin-orbit coupled states, only first 11 low-lying states are shown, as these dominate the magnetic response of the sample.

1		**2_1**		**2_2**		**3**	
Spin-only	Spin-orbit	Spin-only	Spin-orbit	Spin-only	Spin-orbit	Spin-only	Spin-orbit
0.00	0.00	0.00	0.00	0.00	0.00	0.00	0.00
296.57	0.01	385.22	0.02	333.55	0.01	292.24	0.00
3002.55	172.59	2816.04	161.39	2908.07	168.38	2845.81	172.83
3362.74	173.43	3385.96	161.62	3271.89	168.43	3425.28	173.48
5319.69	272.53	5593.09	245.33	5438.98	261.05	5370.12	273.34
20490.38	566.64	20150.22	627.23	20242.73	591.79	20386.84	562.90
20626.69	666.02	20175.09	712.70	20261.83	687.30	20500.98	662.29
20748.12	673.54	20555.48	717.13	20492.97	689.27	20789.54	671.31
[…x41]	853.29	[…x41]	887.70	[…x41]	868.00	[…x41]	850.73
62557.69	853.72	62587.01	888.20	62409.46	868.50	62582.89	851.16
31108.47	3203.21	30798.84	3015.83	30853.12	3102.10	31051.88	3071.35
31512.91		31252.49		31326.42		31406.11	
31549.29		31315.94		31372.18		31513.79	
[…x46]		[…x46]		[…x46]		[…x46]	
114900.56		114922.90		114865.5		114852.91	
4_1		**4_2**		**4_3**		**5**	
Spin-only	Spin-orbit	Spin-only	Spin-orbit	Spin-only	Spin-orbit	Spin-only	Spin-orbit
0.00	0.00	0.00	0.00	0.00	0.00	0.00	0.00
397.47	0.02	329.88	0.01	314.84	0.01	310.37	0.01
2796.52	158.61	2905.29	167.73	2789.22	169.21	2756.95	169.64
3273.88	160.20	3191.07	169.20	3258.14	170.20	3167.23	171.08
5883.79	241.07	5602.98	261.48	5741.36	265.13	5576.82	266.76
19964.29	635.10	20148.44	588.63	20032.27	576.59	20075.05	574.26
19995.31	719.11	20163.64	684.92	20168.53	670.26	20121.21	672.15
20454.92	722.14	20488.59	686.05	20400.40	681.90	20475.91	677.28
[…x41]	891.37	[…x41]	865.24	[…x41]	857.50	[…x41]	856.95
62772.84	891.86	62585.57	865.73	62811.62	857.88	62597.35	857.46
30631.27	2983.88	30791.82	3085.87	30711.15	3002.83	30759.99	2964.27
31053.05		31215.36		31166.67		31185.84	
31147.94		31319.99		31232.25		31233.43	
[…x46]		[…x46]		[…x46]		[…x46]	
115150.70		115046.38		115015.71		115039.4	

Table S6: Effective spin Hamiltonian parameters calculated for the lowest Pseudo Spin Multiplet (S = 2) from RASSI wave functions (approach detailed in Table S4). For **2** and **4**, which feature 2 and 3 distinct molecules in the asymmetric unit respectively, ZFS parameters are provided for all crystal geometries.

Compound	g_x	g_y	g_z	D (cm^{-1})	E (cm^{-1})
1	1.92	1.93	3.08	−63.65	0.16
2$_1$	1.96	1.96	3.01	−58.12	−0.04
2$_2$	1.94	1.94	3.06	−61.35	−0.01
3	1.92	1.93	3.08	−63.78	0.12
4$_1$	1.96	1.97	3.00	−57.21	0.29
4$_2$	1.93	1.95	3.06	−61.42	0.28
4$_3$	1.93	1.94	3.06	−62.12	0.18
5	1.93	1.94	3.07	−62.44	0.28

Table S7: Energies (cm^{-1}) of spin-only and spin-orbit coupled states for **1** calculated by the CASSCF and CASPT2 methods detailed above.

CASSCF					CASPT2	
Spin-only			Spin-orbit		Spin-orbit	
S	Roots	Energy	root	Energy	root	Energy
5	1	0	1	0	1	0
	2	296.57	2	0.01	2	0
	3	3002.55	3	172.59	3	168.4
	4	3362.74	4	173.43	4	169.09
	5	5319.69	5	272.53	5	266.78
3	1	20490.38	6	566.64	6	561.11
	2	20626.69	7	666.02	7	662.57
	3	20748.12	8	673.54	8	669.42
	[…]	x41	9	853.29	9	855.19
	45	62557.69	10	853.72	10	855.36
1	1	31108.47	11	3203.21	11	3198.85
	2	31512.91			[…]	
	3	31549.29			25	5690.348
	[…]					
	50	114900.6				

Table S8: Comparison of ZFS parameters for **1** calculated by CASSCF and CASPT2 methods

	CASSCF	NEVPT2
g_x	1.921443	1.921154
g_y	1.930523	1.929915
g_z	3.080781	3.081513
D (cm^{-1})	-63.647	-62.218
E (cm^{-1})	0.161	0.130

S7 – Magnetic Characterisation

S7.1 – Methodology

All magnetic susceptibility measurements were performed on an MPMS-XL SQUID magnetometer. Finely ground, polycrystalline samples of **1**–**5** were loaded into borosilicate glass tubes (internal diameter 5 mm). To prevent sample torquing solid eicosane was added on top of the samples and melted at 40 °C, then frozen. All samples were then flame sealed under vacuum. The quantities of compound and eicosane used in each sample are provided in Table S9.

All samples were stored at room temperature. Magnetic susceptibility measurements (χ_mT, Figure 3) were performed at 1000 Oe between 2–300 K in zero field cooled conditions. Magnetisation data were collected at 2, 3, 5, and 10 K at fields of 0–40 kOe (1 kOe increments 0–10 kOe, 2.5 kOe increments 10–40 kOe; Figure S24), and between 1.8−5.0 K at fields of 10, 20, 30, and 40 kOe (Figure S26–S30). Hysteresis measurements were performed at 1.8 K between ±10 kOe with a sweep rate of approximately 67 Oe s^{-1} (Figures S31–S35). All DC magnetisation data were corrected for diamagnetic contributions arising from the sample and eicosane using Pascal's constants.[10] AC magnetic susceptibility measurements were performed using a 3.75 Oe switching field. The CC-FIT2 software package[11] was used to fit all AC susceptibility data to the generalised Debye model to determine relaxation times (τ) and subsequently to fit the temperature dependence of these relaxation times.

For the susceptibility curves, we note that the data have three distinct regimes for all compounds: a negative slope between 300 and *ca* 100 K, which is governed by a strong anisotropy in terms of large axial terms (D) and g-tensors in the ZFS Hamiltonian; a positive slope between *ca* 80 and 5 K, which for a fixed set of D and g values can be better reproduced increasing the absolute value of the rhombic parameter (|E|); finally, a more pronounced positive slope between 5 and 2 K. The last two cannot be concomitantly accounted for with |E|, as better agreement in the 80 and 5 K regime leads to inconsistently smaller ChiT values in the 5 and 2 K range. An improvement in both regimes, although admittedly not perfect, can only be achieved by assigning the drop at the coldest temperatures to an antiferromagnetic mean field interaction. This affords smaller E values than those required to reproduce the 80 and 5 K regime on its own, which are more in agreement with CASSCF-SO values, while also making use of reasonably small intramolecular antiferromagnetic interactions.

Table S9: Quantities of sample and eicosane (mg) used in each flame-sealed SQUID magnetometry sample

Compound	R	Sample mass (mg)	Eicosane mass (mg)
1	*t*Bu	31.3	34.3
2	$SiMe_3$	15.0	30.4
3	H	53.6	47.6
4	Cl	32.1	33.8
5·$(C_6H_{14})_{0.5}$	CF_3	20.3	29.4

S7.2 – Static Magnetic Characterisation

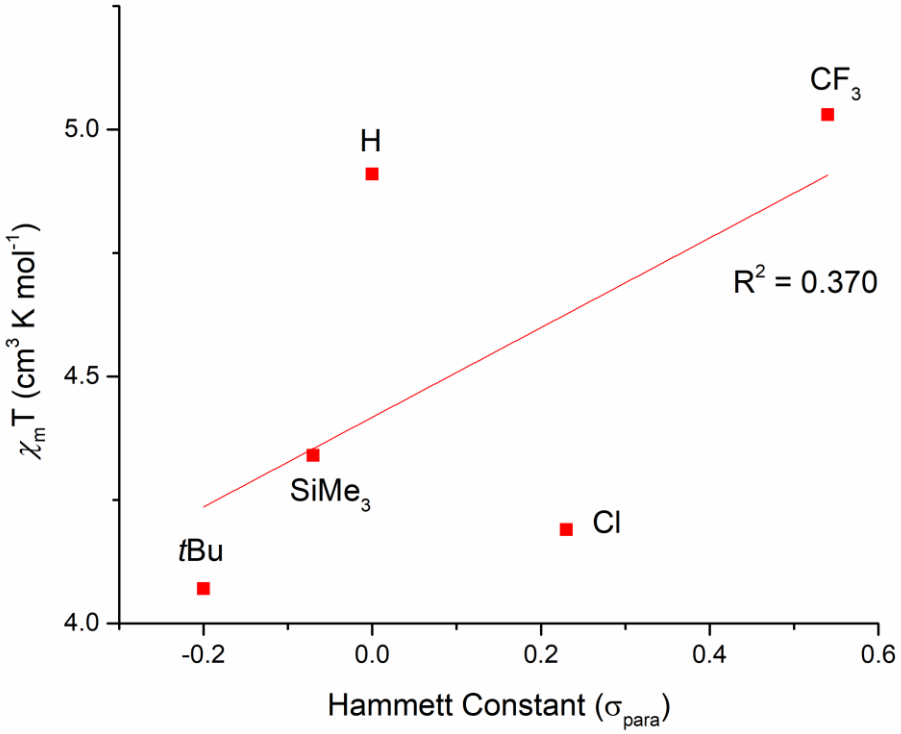

Figure S23: Plot of $\chi_m T$ at 300 K for **1**–**5** versus the Hammett constant $(\sigma_{para})^5$ of their R substituent (*t*Bu, $SiMe_3$, H, Cl, CF_3). Red line represents a linear fit of the data.

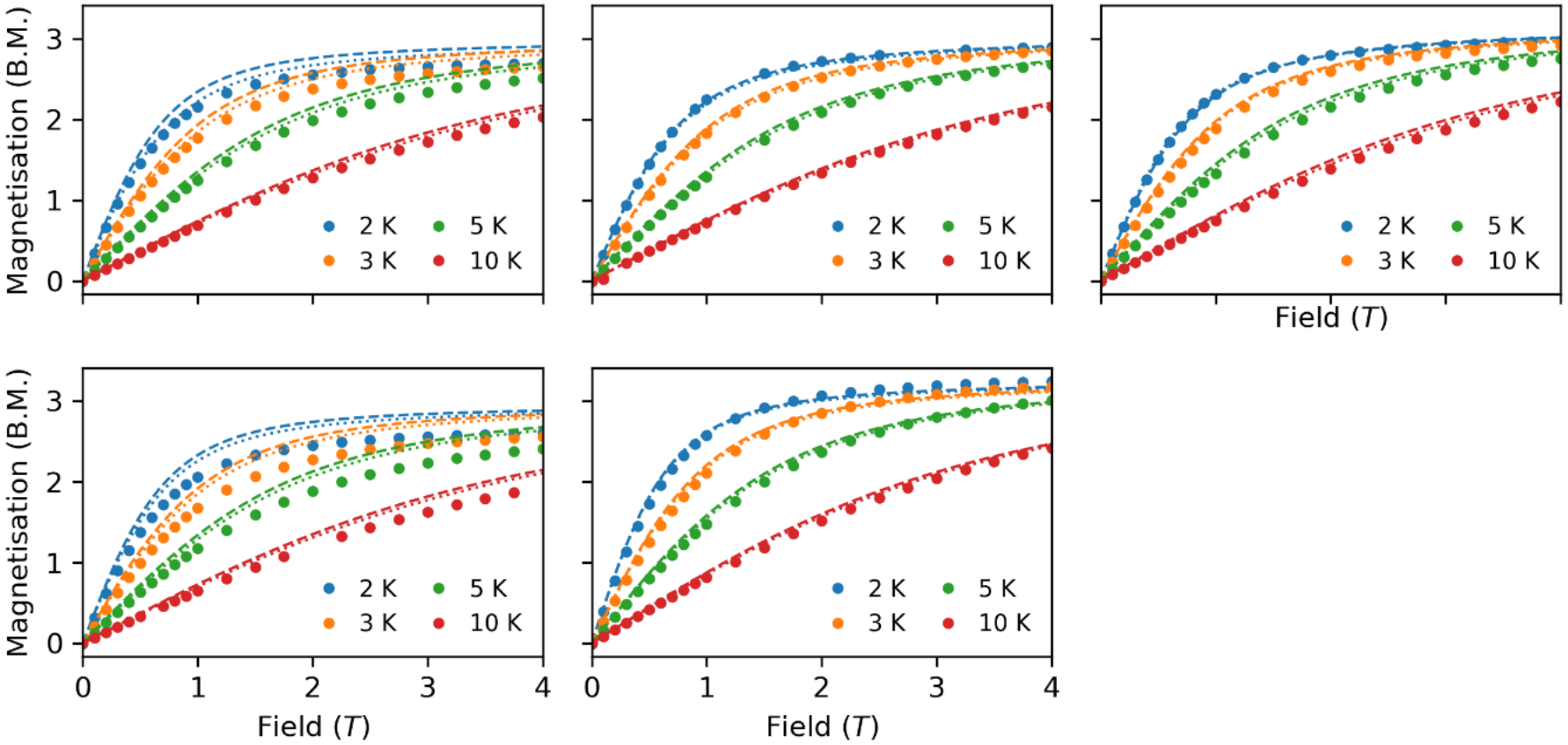

Figure S24: Comparison of experimental (dots) and fitted (lines) magnetisation (*M* vs *H*) curves for **1**–**5**. Dashed and dotted lines refer to *fit1* and *fit2* (Table SX and SY) respectively. Subplots ordered **1**, **2**, **3** (top row, starting upper left), **4**, **5** (bottom rom, starting lower left).

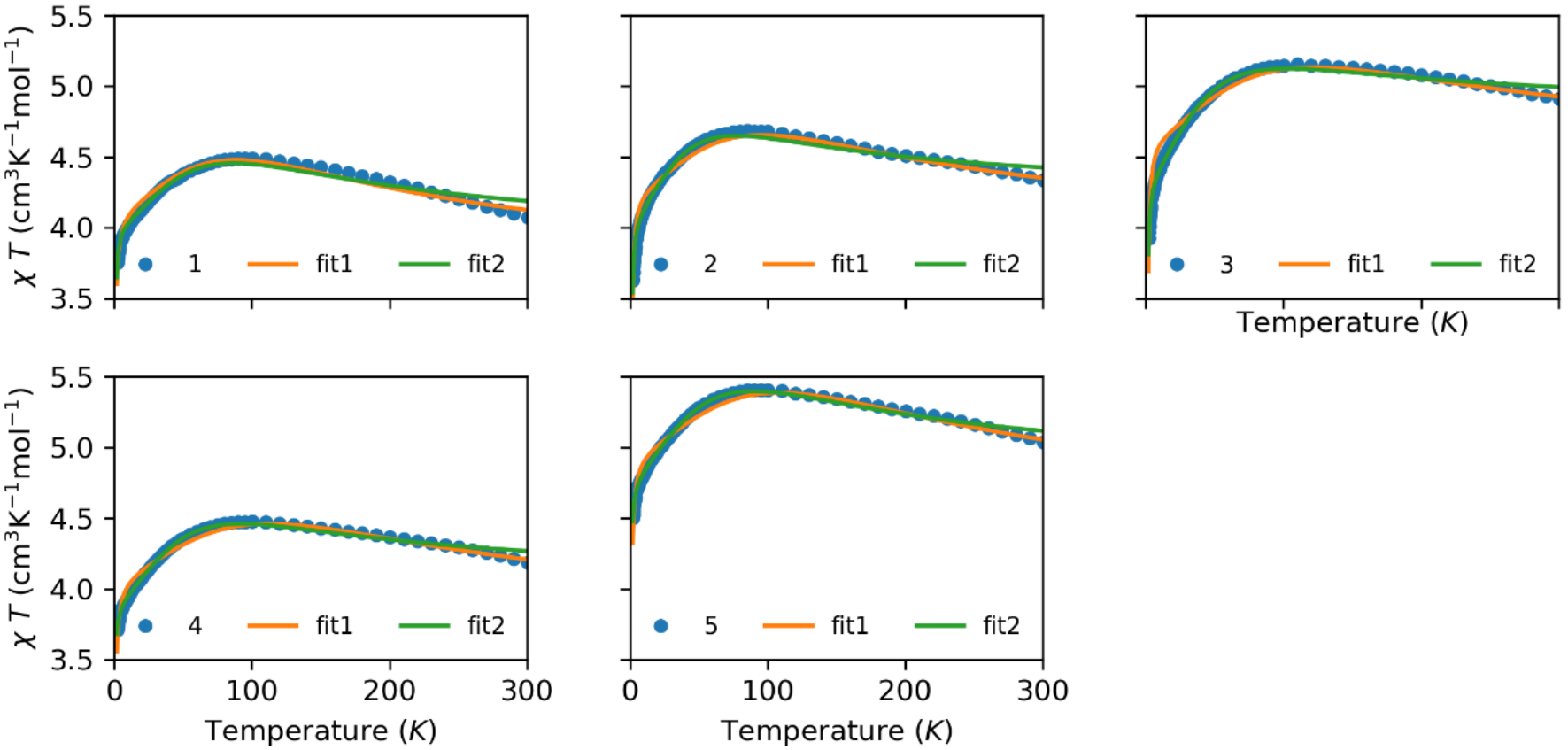

Figure S25: Comparison of experimental (dots) and fitted (solid lines; fit 1 = orange, fit 2 = green) susceptibility traces for **1**–**5**.

Table S10: Zero-field splitting Hamiltonian parameters for **1**–**5** determined using the procedure *fit2* as described as in the main text. Fitting conducted using PHI.[12]

	g_x	g_y	g_z	D (cm^{-1})	E (cm^{-1})	zJ (cm^{-1})
1	1.95	1.95	2.82	-48.17	4.46	-1.6E-02
2	2.10	2.10	2.84	-35.43	-4.42	-7.3E-03
3	2.30	2.30	2.94	-38.44	4.47	-2.1E-03
4	2.05	2.05	2.78	-43.17	1.98	-1.7E-02
5	2.20	2.20	3.08	-46.67	2.28	-9.9E-03

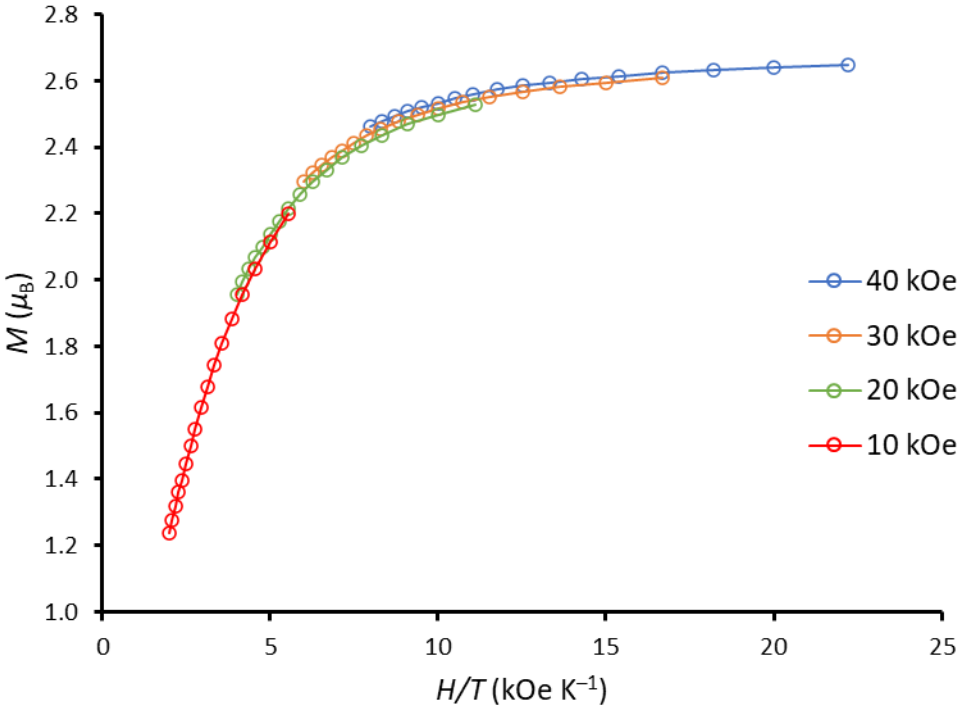

Figure S26: Low temperature magnetisation data for **1** collected at 1.8–5.0 K under DC fields of 10, 20, 30, and 40 kOe. Lines are intended as guides for eyes.

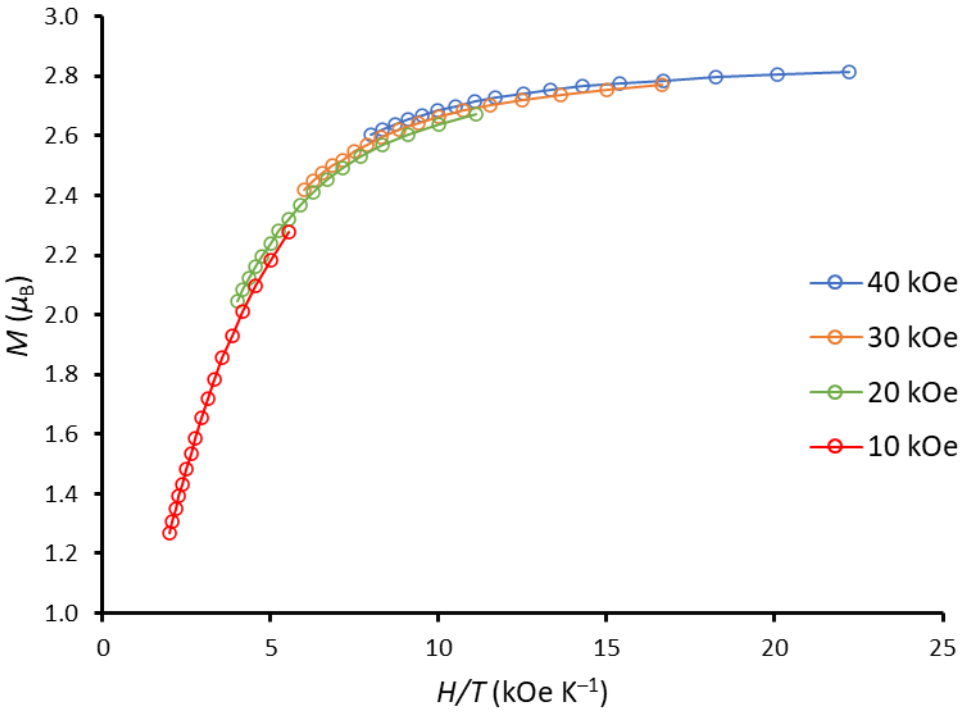

Figure S27: Low temperature magnetisation data for **2** collected at 1.8–5.0 K under DC fields of 10, 20, 30, and 40 kOe. Lines are intended as guides for eyes.

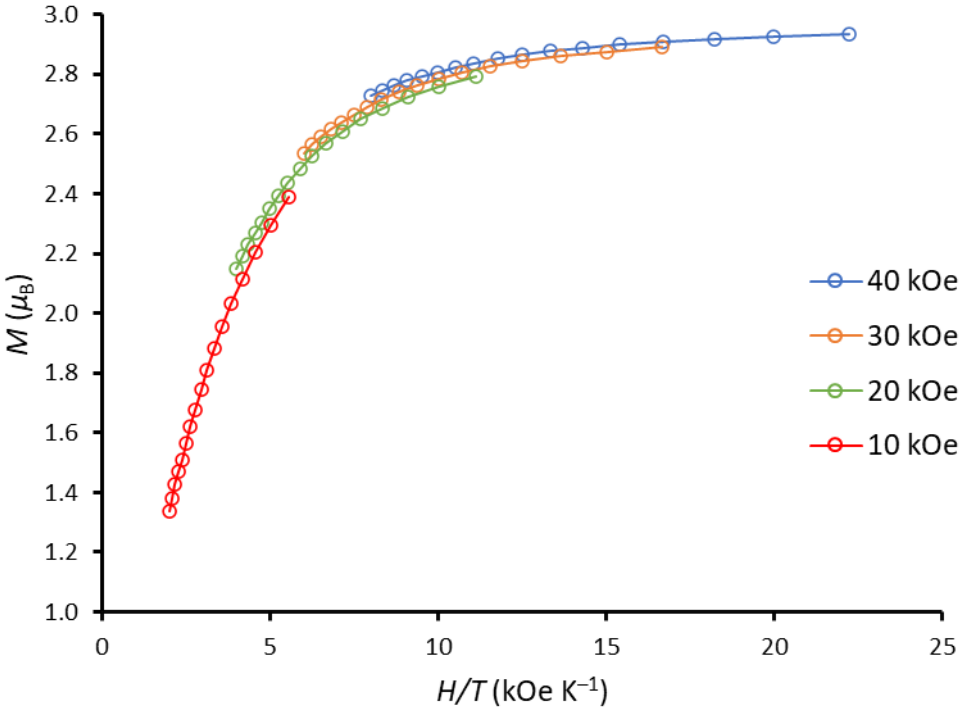

Figure S28: Low temperature magnetisation data for **3** collected at 1.8–5.0 K under DC fields of 10, 20, 30, and 40 kOe. Lines are intended as guides for eyes.

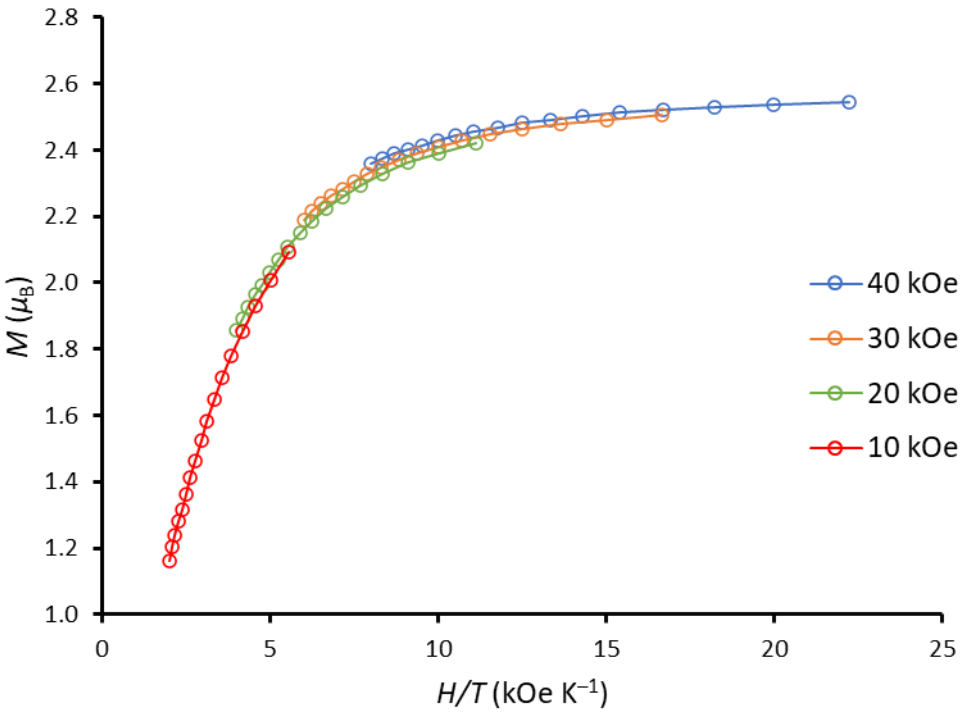

Figure S29: Low temperature magnetisation data for **4** collected at 1.8–5.0 K under DC fields of 10, 20, 30, and 40 kOe. Lines are intended as guides for eyes.

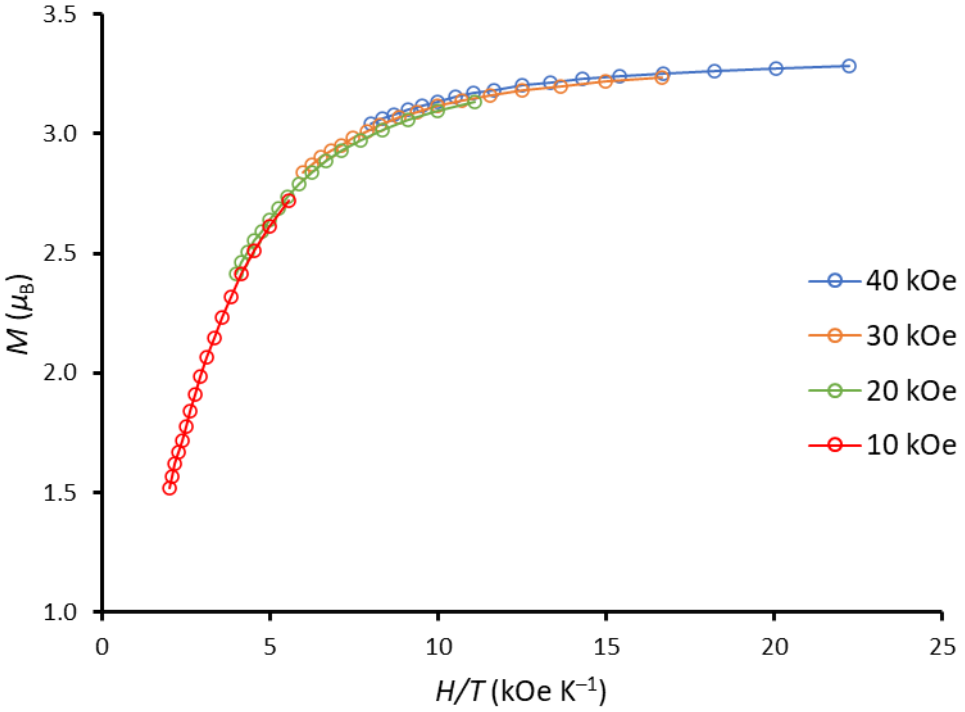

Figure S30: Low temperature magnetisation data for **5** collected at 1.8–5.0 K under DC fields of 10, 20, 30, and 40 kOe. Lines are intended as guides for eyes.

S7.3 – Hysteresis Measurements

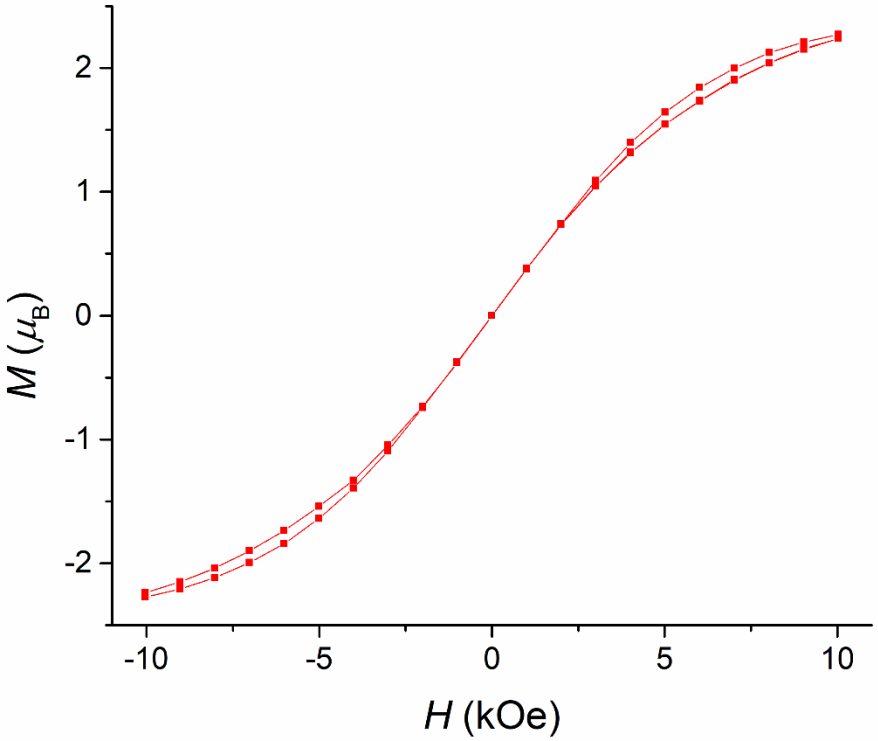

Figure S31: Hysteresis measurement for **1** recorded at 1.8 K at 67 Oe s^{-1}.

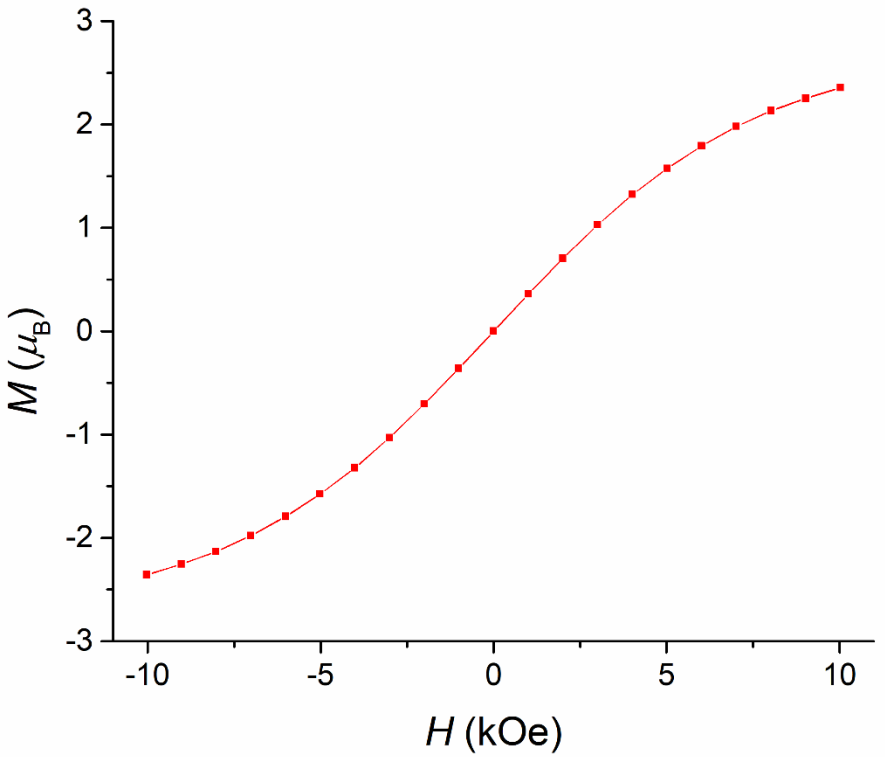

Figure S32: Hysteresis measurement for **2** recorded at 1.8 K at 67 Oe s^{-1}.

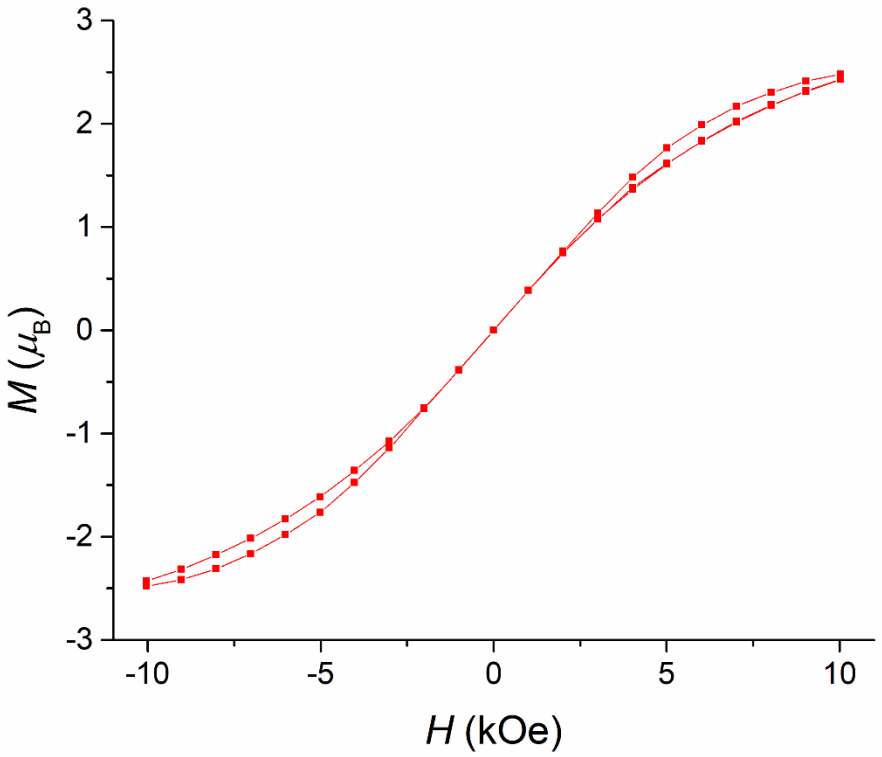

Figure S33: Hysteresis measurement for **3** recorded at 1.8 K at 67 Oe s^{-1}.

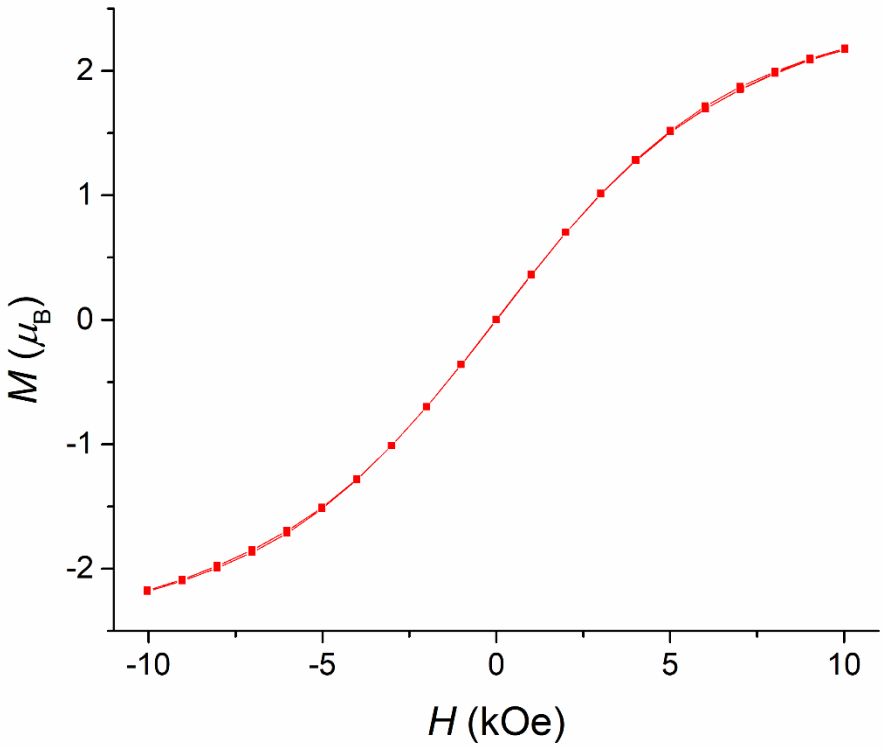

Figure S34: Hysteresis measurement for **4** recorded at 1.8 K at 67 Oe s^{-1}.

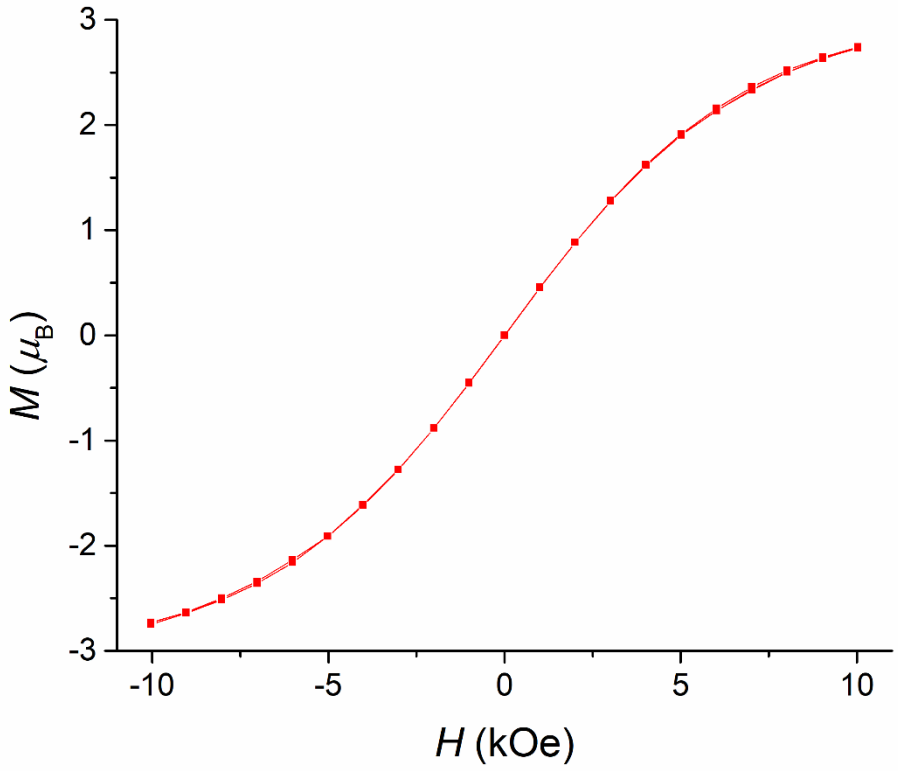

Figure S35: Hysteresis measurement for **5** recorded at 1.8 K at 67 Oe s^{-1}.

S7.4 – AC Susceptibility Data

S7.4.1 – Variable Field, Fixed Temperature

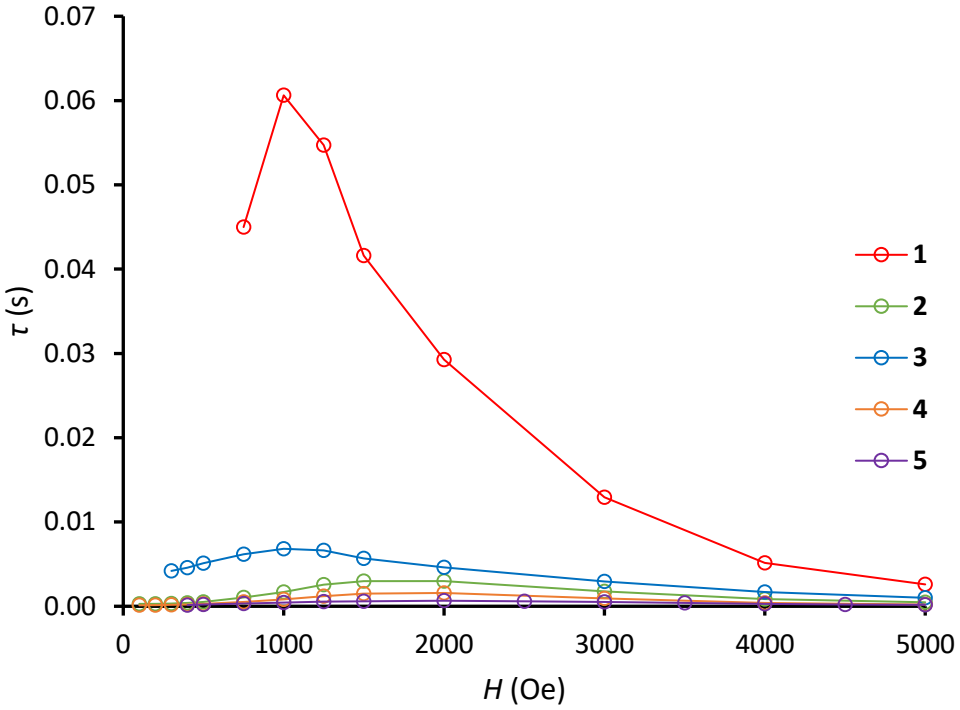

Figure S36: Plot of relaxation time (τ) as a function of field (H) for complexes **1**–**5** at 2 K. AC susceptibility data recorded over 1–1400 Hz. Lines are intended as guides for eyes.

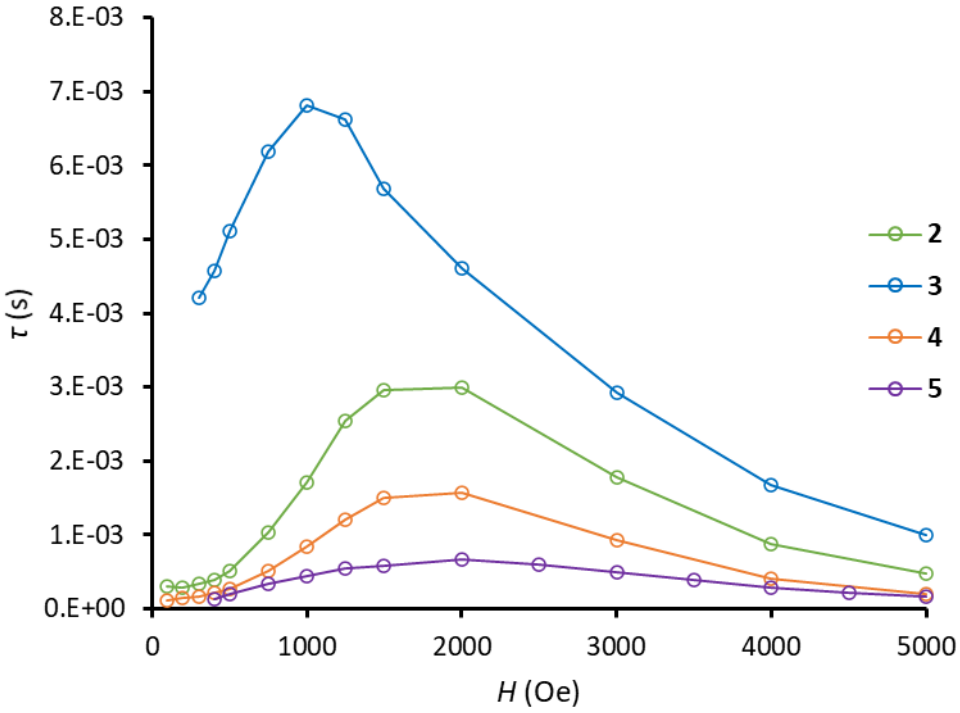

Figure S37: Plot of relaxation time (τ) as a function of field (H) for complexes **2**–**5** at 2 K. AC susceptibility data recorded over 1–1400 Hz. Lines are intended as guides for eyes.

S7.4.2 – Variable Temperature, Fixed Field

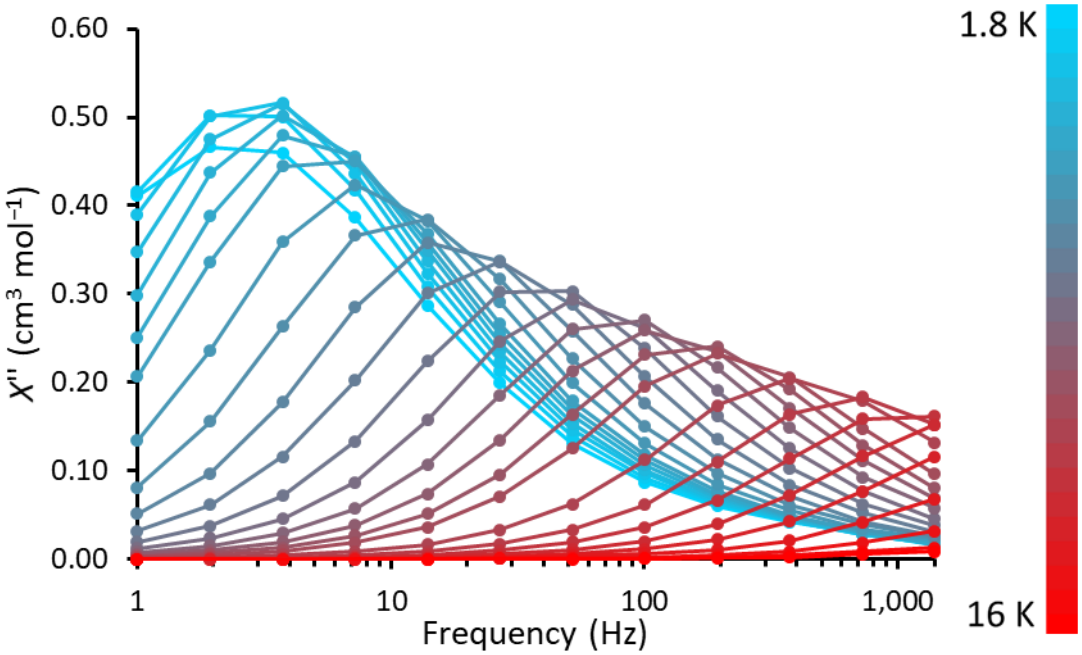

Figure S38: Frequency dependence of the out-of-phase AC susceptibilities (χ'') for **1** under a 1000 Oe DC field. Lines are intended as guides for eyes.

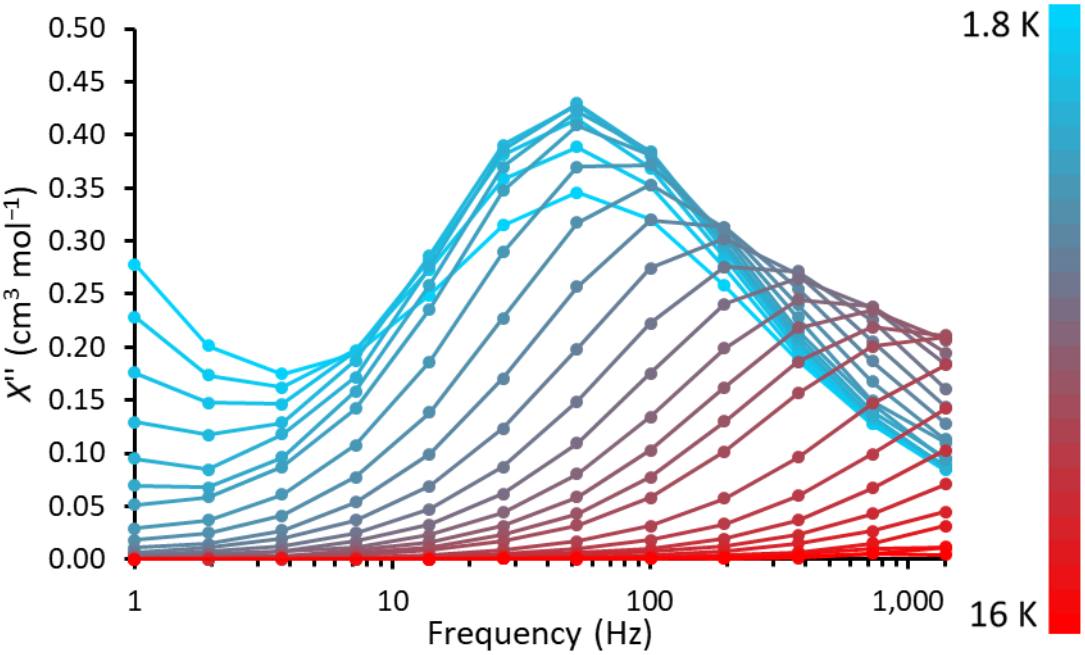

Figure S39: Frequency dependence of the out-of-phase AC susceptibilities (χ'') for **2** under a 1750 Oe DC field. Lines are intended as guides for eyes.

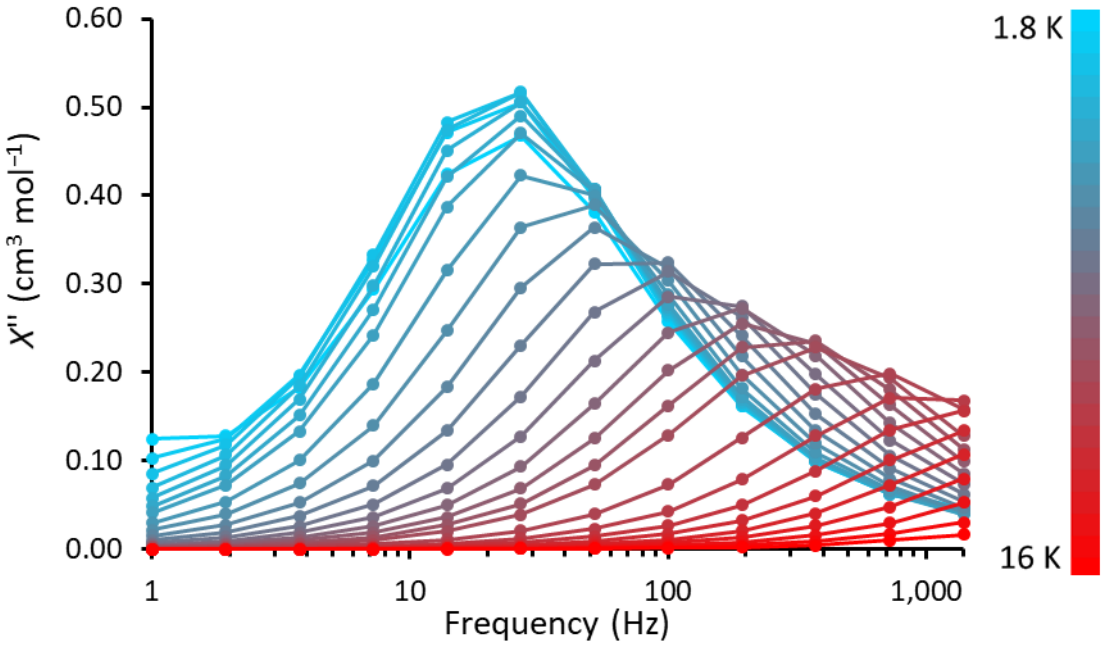

Figure S40: Frequency dependence of the out-of-phase AC susceptibilities (χ'') for **3** under a 1000 Oe DC field. Lines are intended as guides for eyes.

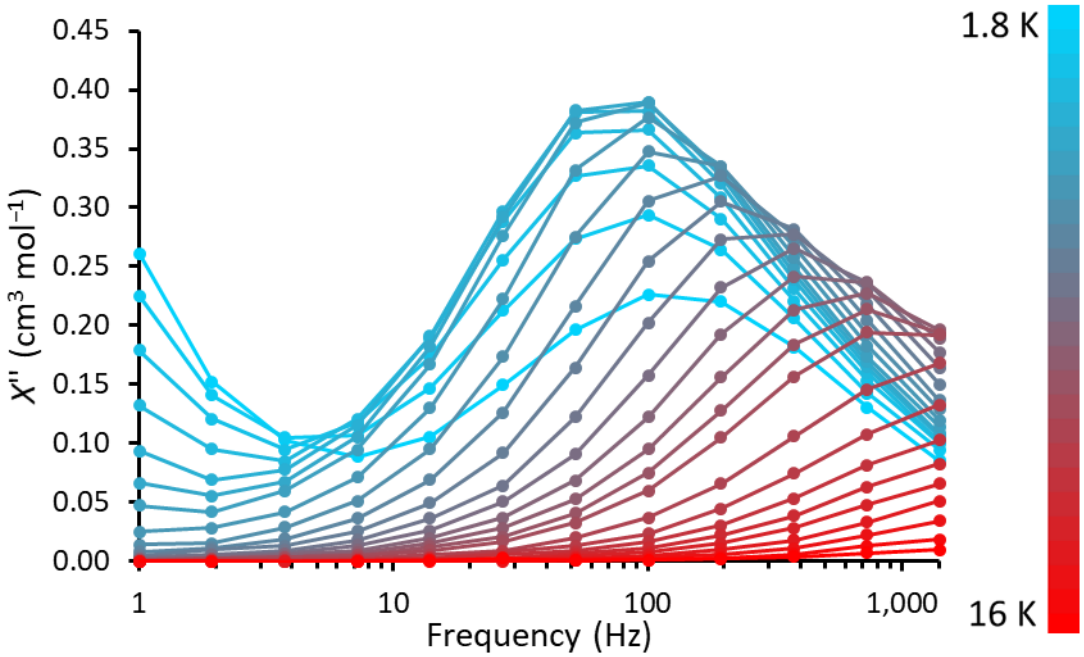

Figure S41: Frequency dependence of the out-of-phase AC susceptibilities (χ'') for **4** under a 2000 Oe DC field. Lines are intended as guides for eyes.

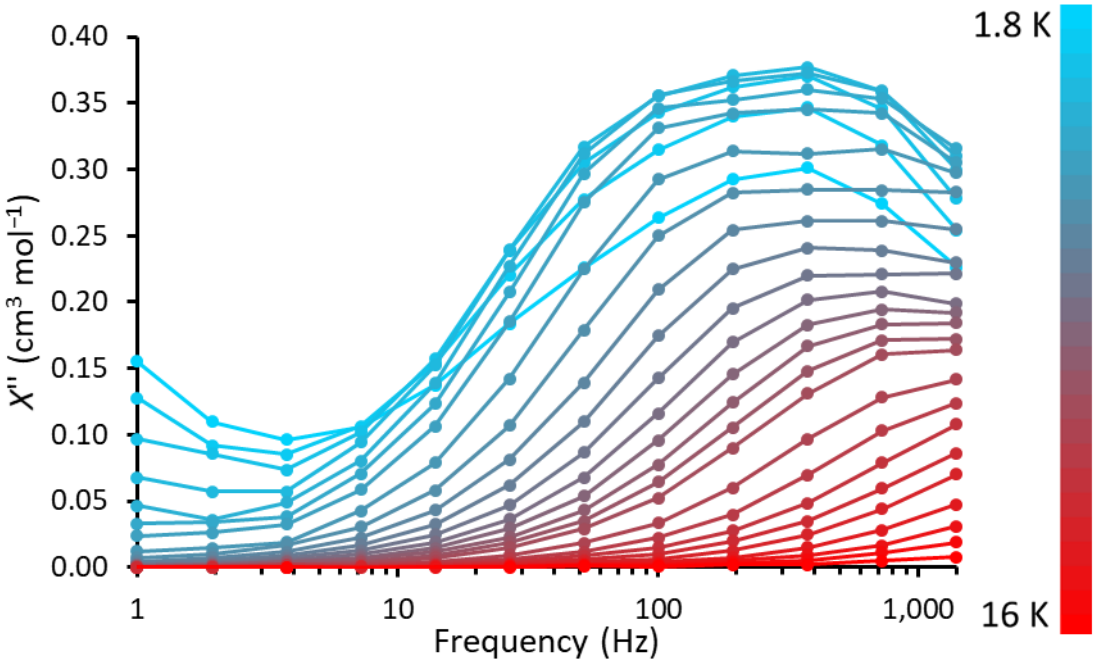

Figure S42: Frequency dependence of the out-of-phase AC susceptibilities (χ'') for **5** under a 2000 Oe DC field. Lines are intended as guides for eyes.

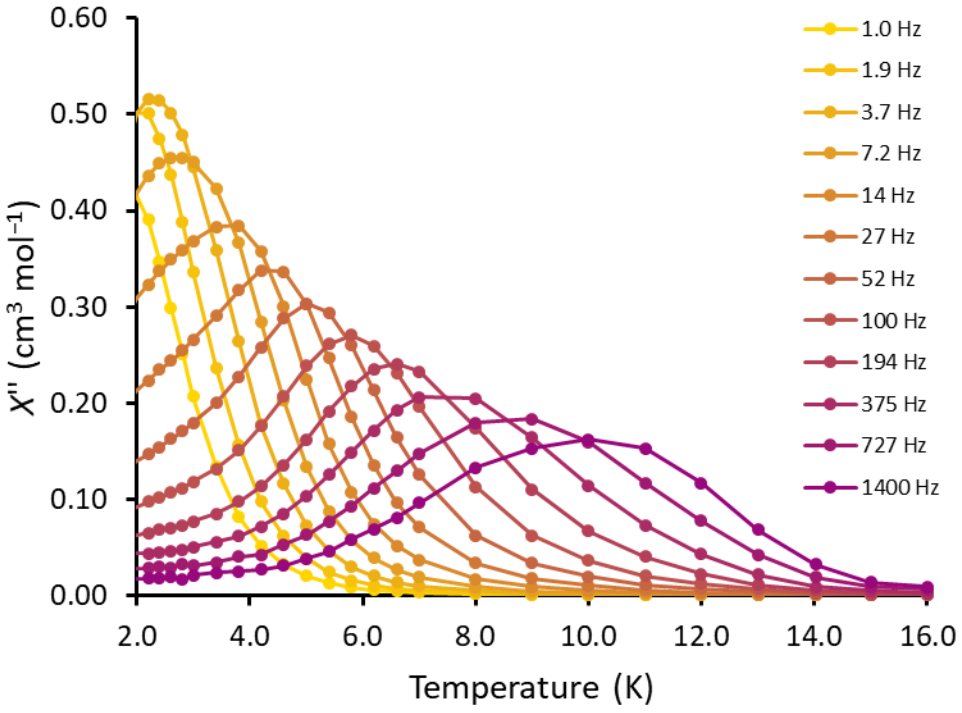

Figure S43: Temperature dependence of the out-of-phase AC susceptibilities (χ'') for **1** under a 1000 Oe DC field. Lines are intended as guides for eyes.

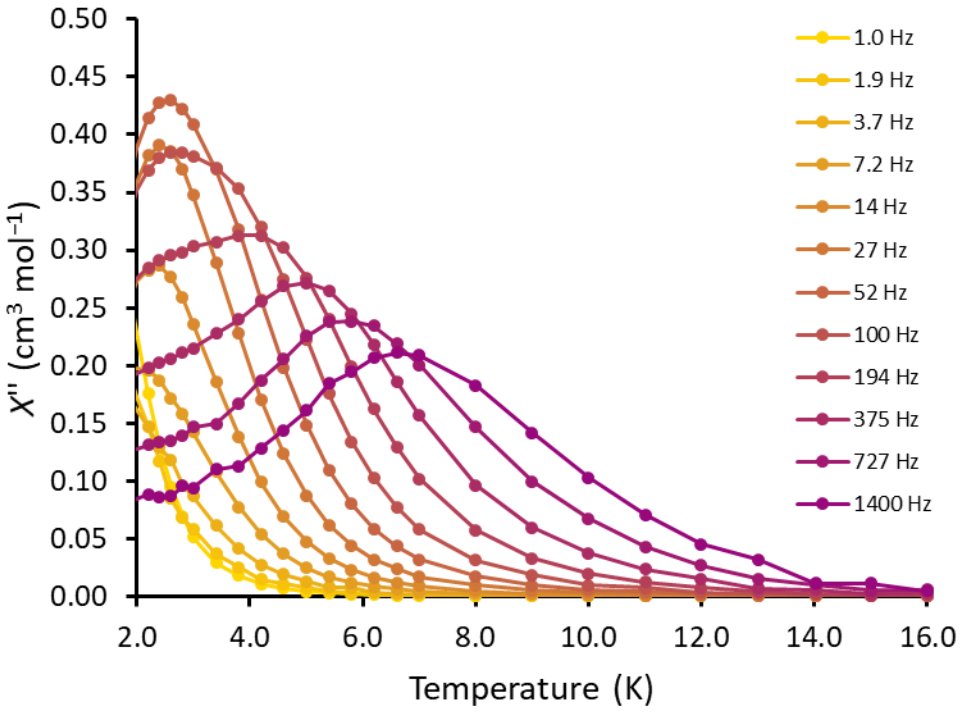

Figure S44: Temperature dependence of the out-of-phase AC susceptibilities (χ'') for **2** under a 1750 Oe DC field. Lines are intended as guides for eyes.

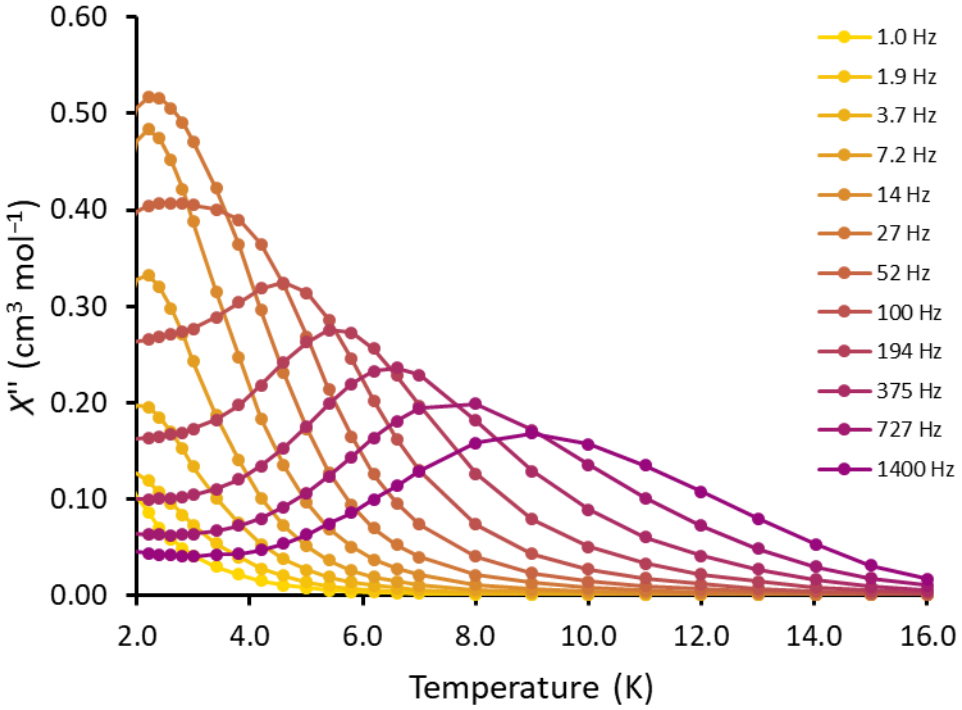

Figure S45: Temperature dependence of the out-of-phase AC susceptibilities (χ'') for **3** under a 1000 Oe DC field. Lines are intended as guides for eyes.

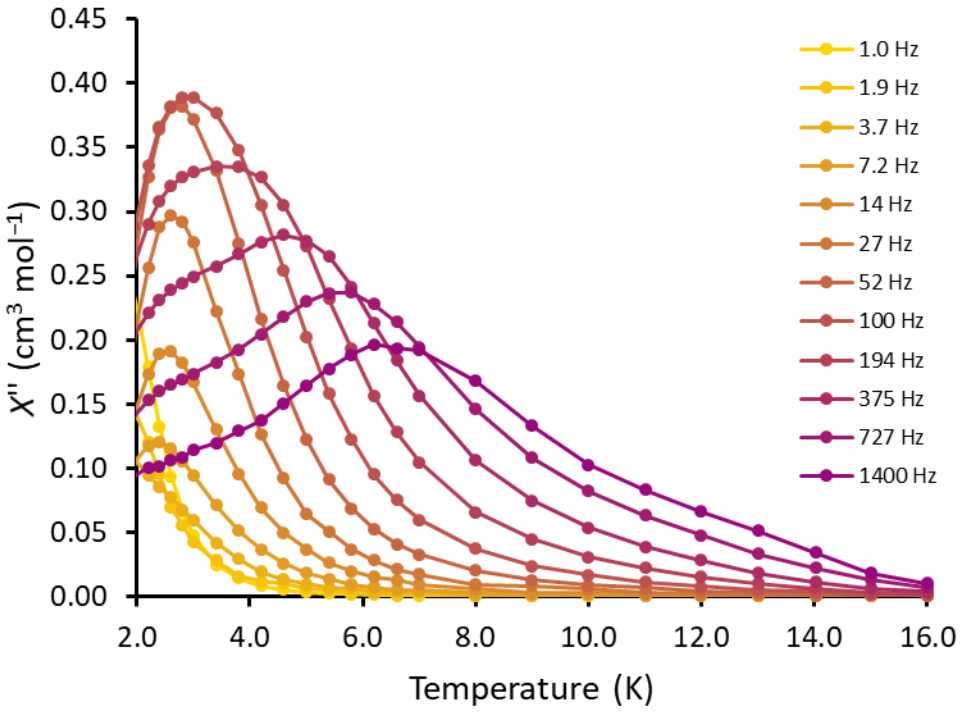

Figure S46: Temperature dependence of the out-of-phase AC susceptibilities (χ'') for **4** under a 2000 Oe DC field. Lines are intended as guides for eyes.

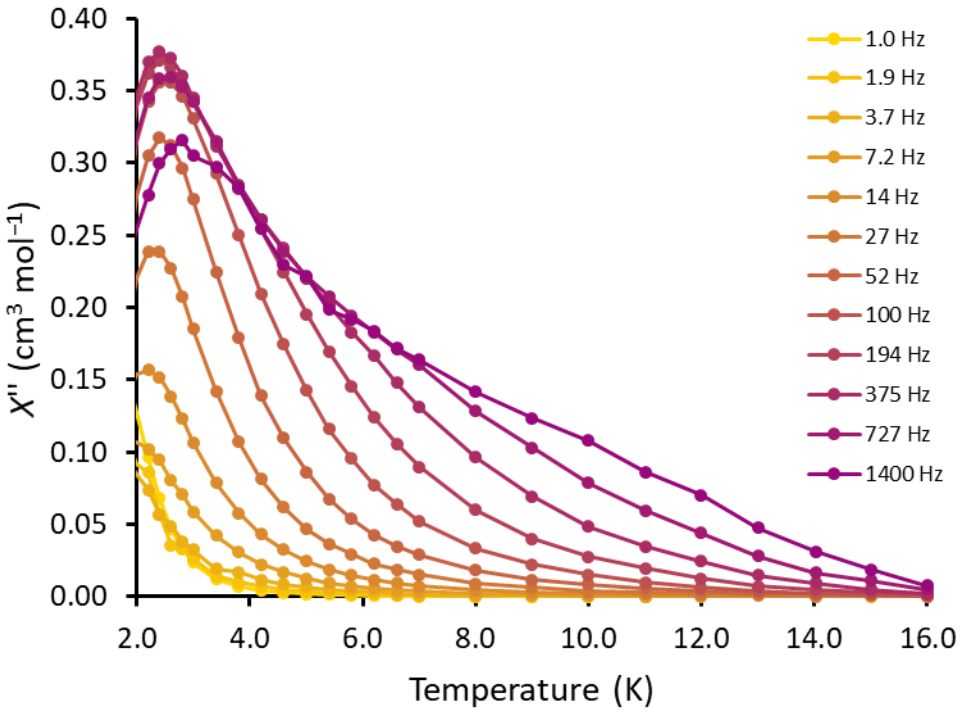

Figure S47: Temperature dependence of the out-of-phase AC susceptibilities (χ'') for **5** under a 2000 Oe DC field. Lines are intended as guides for eyes.

S7.5 – Cole-Cole Plots and General Debye Fitting

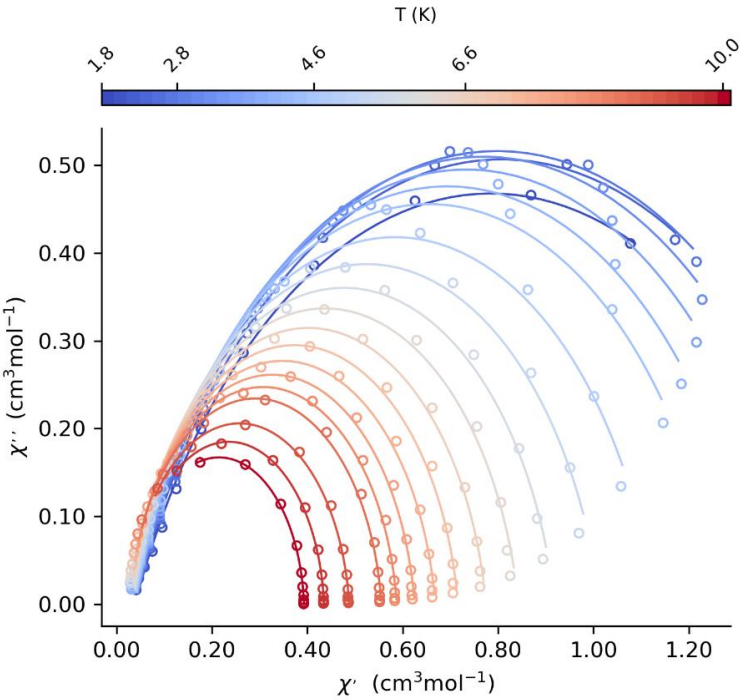

Figure S48: Cole-Cole plots of the frequency dependence (1–1400 Hz) of χ' and χ'' used to evaluate the temperature dependence of τ for **1** at 1000 Oe applied field. Lines represent fits to the general Debye model. Fit conducted and figure generated using the CC-FIT2 software package.[11]

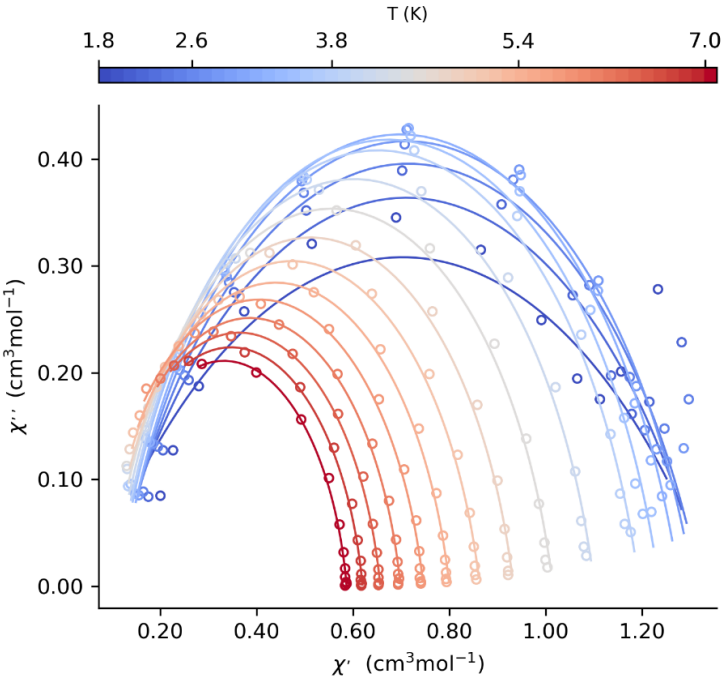

Figure S49: Cole-Cole plots of the frequency dependence (1–1400 Hz) of χ' and χ'' used to evaluate the temperature dependence of τ for **2** at 1750 Oe applied field. Lines represent fits to the general Debye model. Fit conducted and figure generated using the CC-FIT2 software package.[11] Note that fits to the general Debye model at <2.4 K were judged to be poor for **2**, and the determined τ values were not used in further analysis.

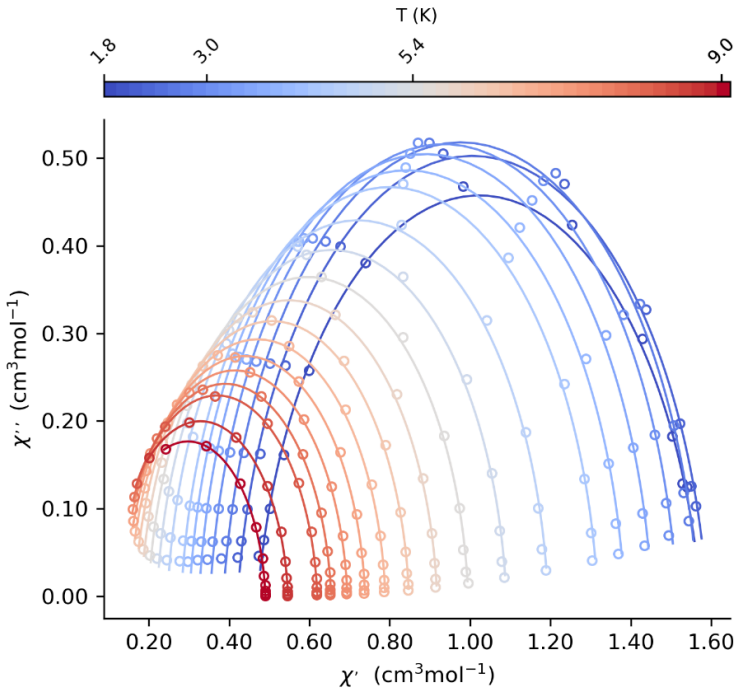

Figure S50: Cole-Cole plots of the frequency dependence (1–1400 Hz) of χ' and χ'' used to evaluate the temperature dependence of τ for **3** at 1000 Oe applied field. Lines represent fits to the general Debye model. Fit conducted and figure generated using the CC-FIT2 software package.[11]

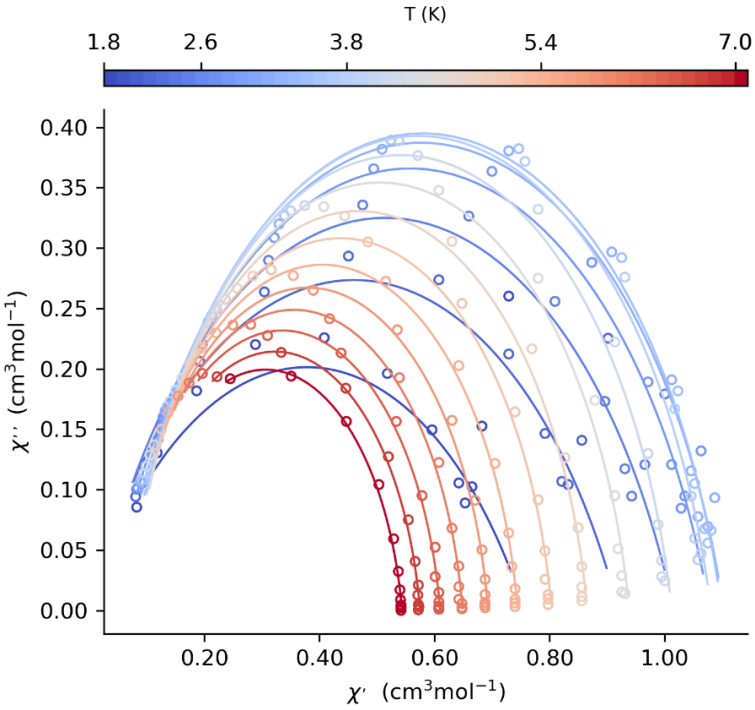

Figure S51: Cole-Cole plots of the frequency dependence (1–1400 Hz) of χ' and χ'' used to evaluate the temperature dependence of τ for **4** at 2000 Oe applied field. Lines represent fits to the general Debye model. Fit conducted and figure generated using the CC-FIT2 software package.[11] Note that fits to the general Debye model at <2.4 K were judged to be poor for **4**, and the determined τ values were not used in further analysis.

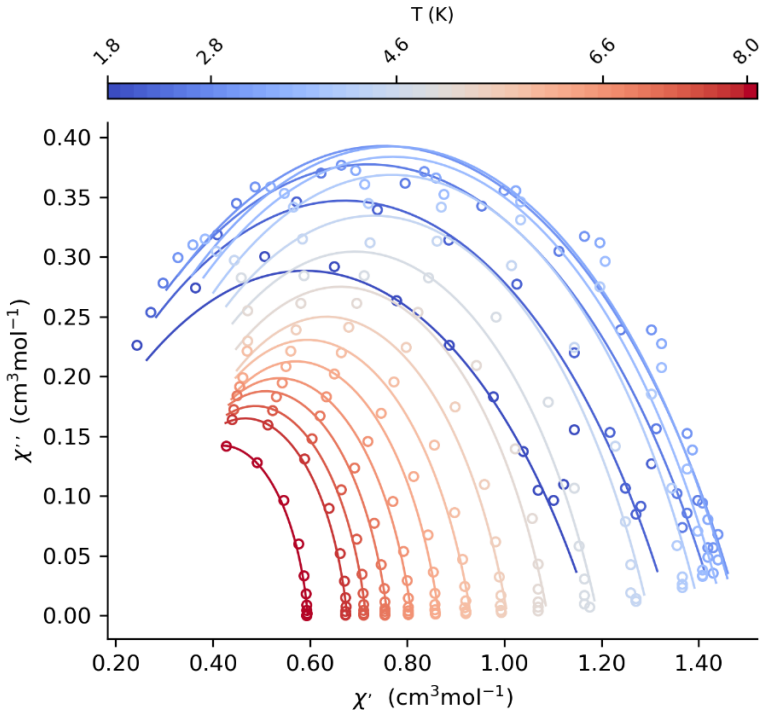

Figure S52: Cole-Cole plots of the frequency dependence (1–1400 Hz) of χ' and χ'' used to evaluate the temperature dependence of τ for **5** at 2000 Oe applied field. Lines represent fits to the general Debye model. Fit conducted and figure generated using the CC-FIT2 software package.[11] Note that fits to the general Debye model at <2.4 K were judged to be poor for **2**, and the determined τ values were not used in further analysis.

Table S11: Best fitted parameters (τ, τ error, α) with general Debye model for **1** at 1000 Oe applied field.

T (K)	τ (s)	τ error (s)	α
1.8	6.66E-02	1.37E-03	0.286
2.0	5.98E-02	1.08E-03	0.257
2.2	5.28E-02	1.10E-03	0.238
2.4	4.51E-02	1.01E-03	0.223
2.6	3.83E-02	9.25E-04	0.211
2.8	3.21E-02	7.63E-04	0.200
3.0	2.69E-02	6.32E-04	0.189
3.4	1.85E-02	4.12E-04	0.169
3.8	1.26E-02	2.74E-04	0.148
4.2	8.48E-03	1.57E-04	0.129
4.6	5.74E-03	1.02E-04	0.117
5.0	3.84E-03	6.10E-05	0.106
5.4	2.64E-03	4.24E-05	0.095
5.8	1.85E-03	2.73E-05	0.091
6.2	1.32E-03	1.86E-05	0.084
6.6	9.72E-04	1.32E-05	0.078
7.0	7.31E-04	1.00E-05	0.076
8.0	3.91E-04	5.86E-06	0.070
9.0	2.38E-04	2.79E-06	0.048
10.0	1.51E-04	2.20E-06	0.041

Table S12: Best fitted parameters (τ, τ error, α) with general Debye model for **2** at 1750 Oe applied field.

T (K)	τ (s)	τ error (s)	α
2.4	3.03E-03	1.27E-04	0.222
2.6	2.87E-03	7.60E-05	0.197
2.8	2.63E-03	5.82E-05	0.185
3.0	2.40E-03	4.65E-05	0.178
3.4	1.92E-03	4.02E-05	0.168
3.8	1.48E-03	2.75E-05	0.164
4.2	1.09E-03	2.28E-05	0.159
4.6	7.92E-04	1.50E-05	0.155
5.0	5.74E-04	1.06E-05	0.149
5.4	4.14E-04	8.69E-06	0.148
5.8	3.15E-04	5.75E-06	0.137
6.2	2.39E-04	5.22E-06	0.132
6.6	1.87E-04	4.51E-06	0.125
7.0	1.50E-04	3.94E-06	0.118

Table S13: Best fitted parameters (τ, τ error, α) with general Debye model for **3** at 1000 Oe applied field.

T (K)	τ (s)	τ error (s)	α
2.4	6.64E-03	8.15E-05	0.076
2.6	6.28E-03	7.47E-05	0.070
2.8	5.85E-03	7.06E-05	0.069
3.0	5.38E-03	6.29E-05	0.066
3.4	4.44E-03	5.04E-05	0.063
3.8	3.55E-03	3.72E-05	0.060
4.2	2.74E-03	2.53E-05	0.056
4.6	2.09E-03	1.76E-05	0.055
5.0	1.57E-03	1.25E-05	0.052
5.4	1.18E-03	8.99E-06	0.051
5.8	9.02E-04	6.34E-06	0.053
6.2	6.94E-04	4.66E-06	0.054
6.6	5.42E-04	3.63E-06	0.053
7.0	4.30E-04	3.45E-06	0.053
8.0	2.55E-04	2.18E-06	0.055
9.0	1.64E-04	1.91E-06	0.055

Table S14: Best fitted parameters (τ, τ error, α) with general Debye model for **4** at 1000 Oe applied field.

T (K)	τ (s)	τ error (s)	α
2.4	1.92E-03	1.17E-04	0.221
2.6	1.89E-03	7.24E-05	0.193
2.8	1.81E-03	5.19E-05	0.173
3.0	1.69E-03	4.35E-05	0.162
3.4	1.38E-03	3.18E-05	0.141
3.8	1.10E-03	2.45E-05	0.129
4.2	8.59E-04	1.83E-05	0.117
4.6	6.66E-04	1.26E-05	0.111
5.0	5.11E-04	9.44E-06	0.108
5.4	3.98E-04	7.58E-06	0.100
5.8	3.12E-04	5.74E-06	0.104
6.2	2.48E-04	4.89E-06	0.107
6.6	2.06E-04	4.41E-06	0.102
7.0	1.68E-04	4.16E-06	0.110

Table S15: Best fitted parameters (τ, τ error, α) with general Debye model for **5** at 1000 Oe applied field.

T (K)	τ (s)	τ error (s)	α
2.4	5.96E-04	4.49E-05	0.374
2.6	5.68E-04	4.65E-05	0.358
2.8	5.27E-04	4.81E-05	0.349
3.0	5.10E-04	4.77E-05	0.332
3.4	4.28E-04	4.40E-05	0.321
3.8	3.70E-04	3.81E-05	0.303
4.2	3.37E-04	3.22E-05	0.271
4.6	3.11E-04	2.52E-05	0.247
5.0	2.64E-04	2.28E-05	0.234
5.4	2.47E-04	1.67E-05	0.203
5.8	2.11E-04	1.47E-05	0.197
6.2	1.86E-04	1.23E-05	0.180
6.6	1.68E-04	1.03E-05	0.164
7.0	1.51E-04	9.59E-06	0.151
8.0	1.14E-04	7.61E-06	0.134

S7.6 – Relaxation Profiles

S7.6.1 – Fitting to direct and Raman relaxation model

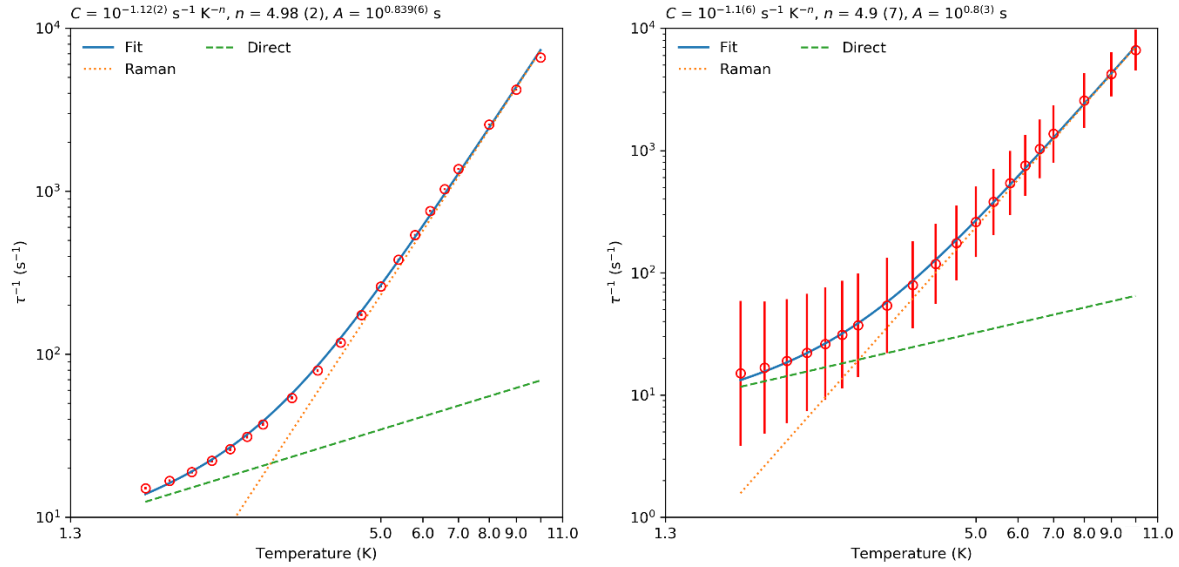

Figure S53: Log-log plots of τ^{-1} vs temperature for complex **1**, recorded at 1000 Oe applied field. Error bars represent either estimated error in fitting of τ from AC susceptibility data by generalised Debye model (left) or ESDs calculated from alpha parameter (right). Fit conducted and figure generated using the CC-FIT2 software package.[11]

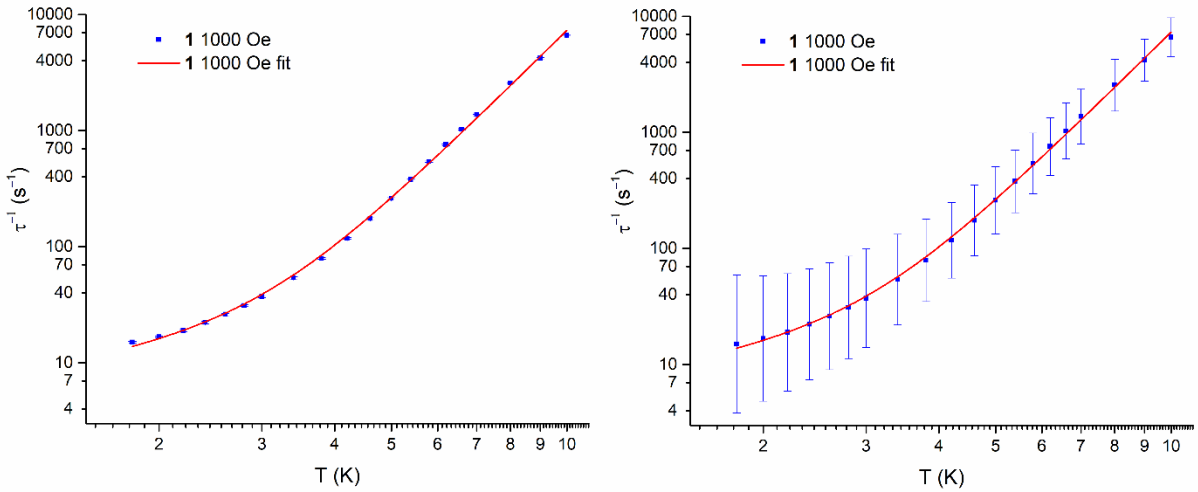

Figure S54: Replot of Figure S53, with identical y-axes for ease of comparison.

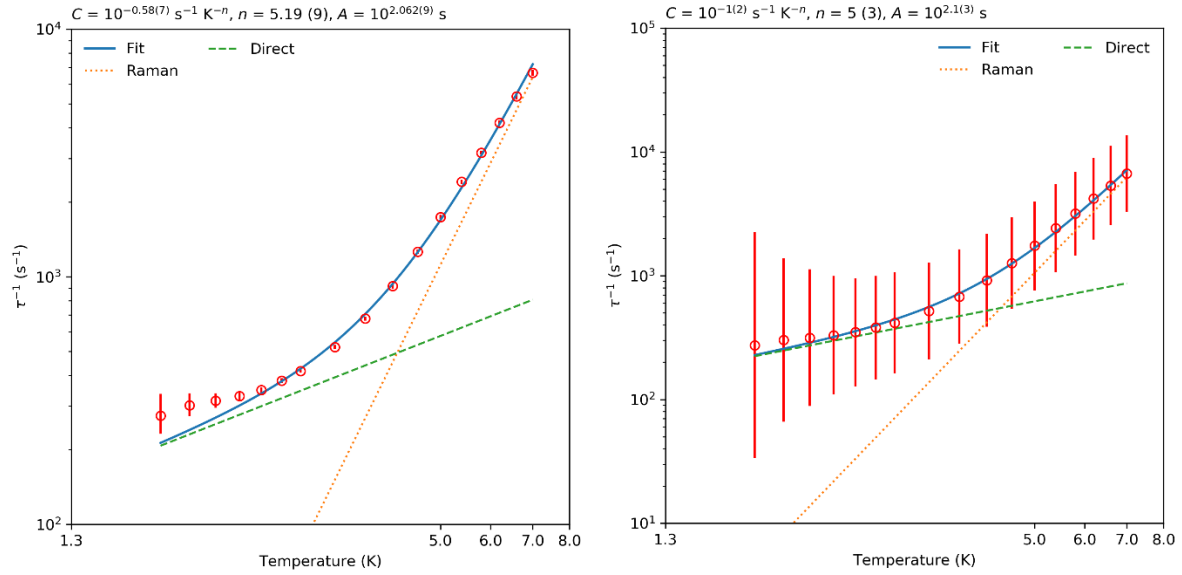

Figure S55: Log-log plots of τ^{-1} vs temperature for complex **2**, recorded at 1750 Oe applied field. Error bars represent either estimated error in fitting of τ from AC susceptibility data by generalised Debye model (left) or ESDs calculated from alpha parameter (right). Fit conducted and figure generated using the CC-FIT2 software package.[11]

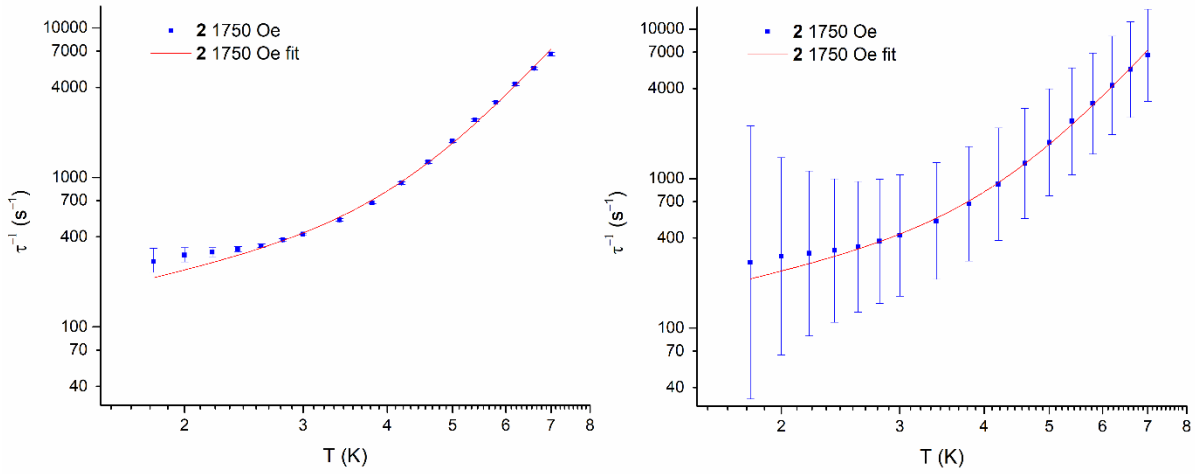

Figure S56: Replot of Figure S55, with identical y-axes for ease of comparison.

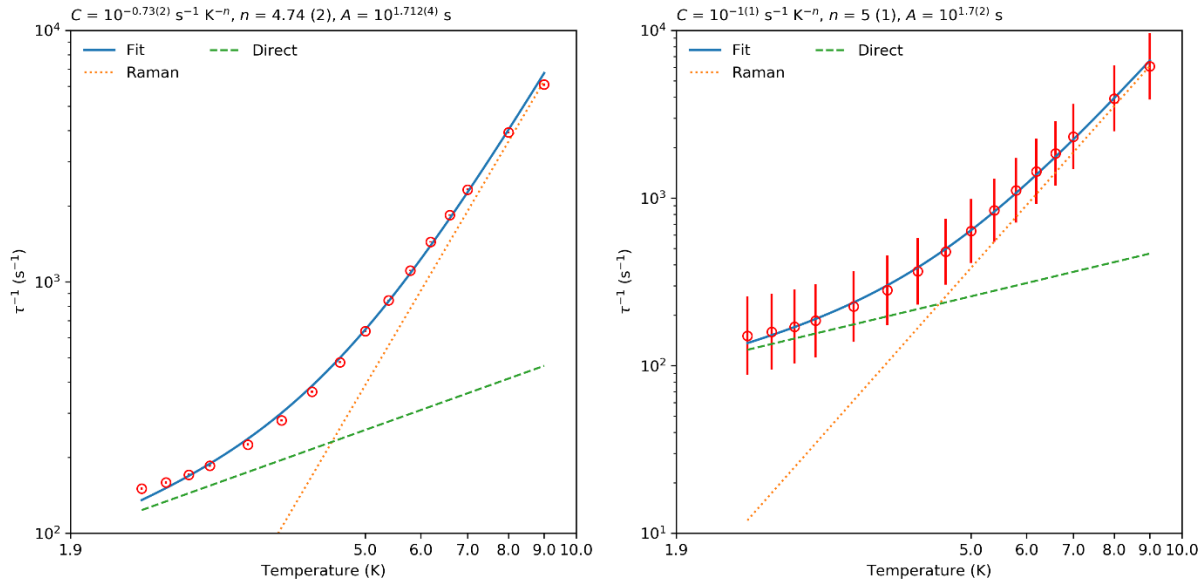

Figure S57: Log-log plots of τ^{-1} vs temperature for complex **3**, recorded at 1000 Oe applied field. Error bars represent either estimated error in fitting of τ from AC susceptibility data by generalised Debye model (left) or ESDs calculated from alpha parameter (right). Fit conducted and figure generated using the CC-FIT2 software package.[11]

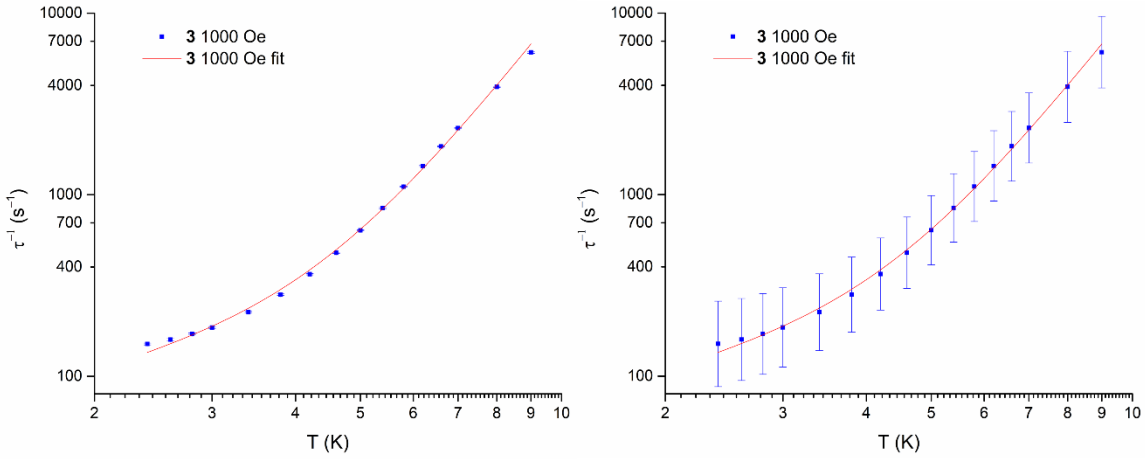

Figure S58: Replot of Figure S57, with identical y-axes for ease of comparison.

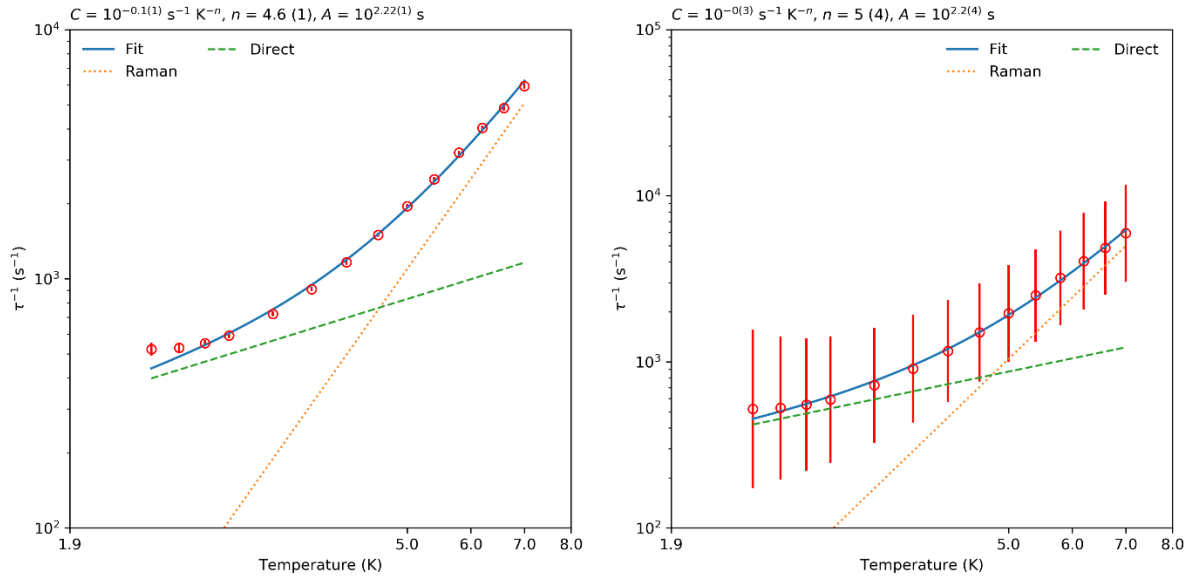

Figure S59: Log-log plots of τ^{-1} vs temperature for complex **4**, recorded at 2000 Oe applied field. Error bars represent either estimated error in fitting of τ from AC susceptibility data by generalised Debye model (left) or ESDs calculated from alpha parameter (right). Fit conducted and figure generated using the CC-FIT2 software package.[11]

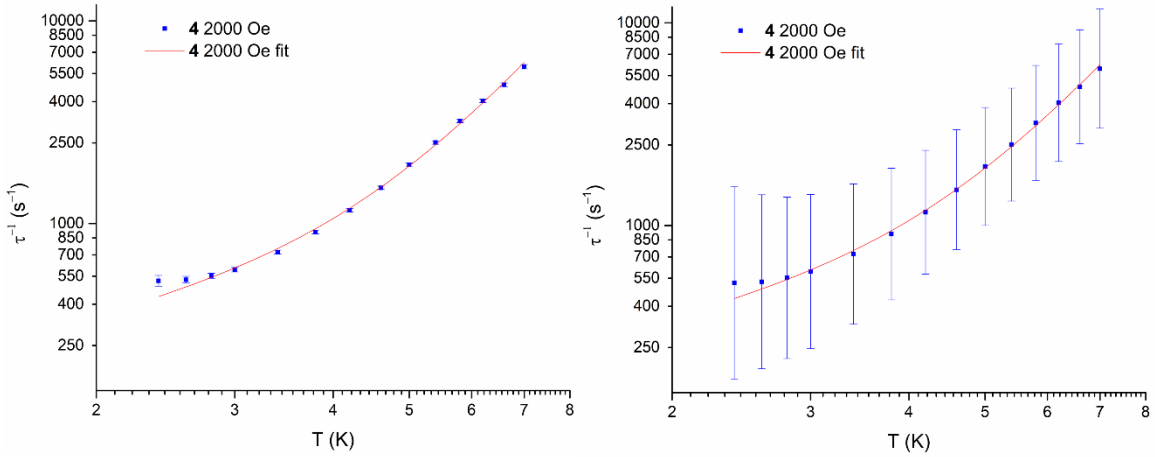

Figure S60: Replot of Figure S59, with identical y-axes for ease of comparison.

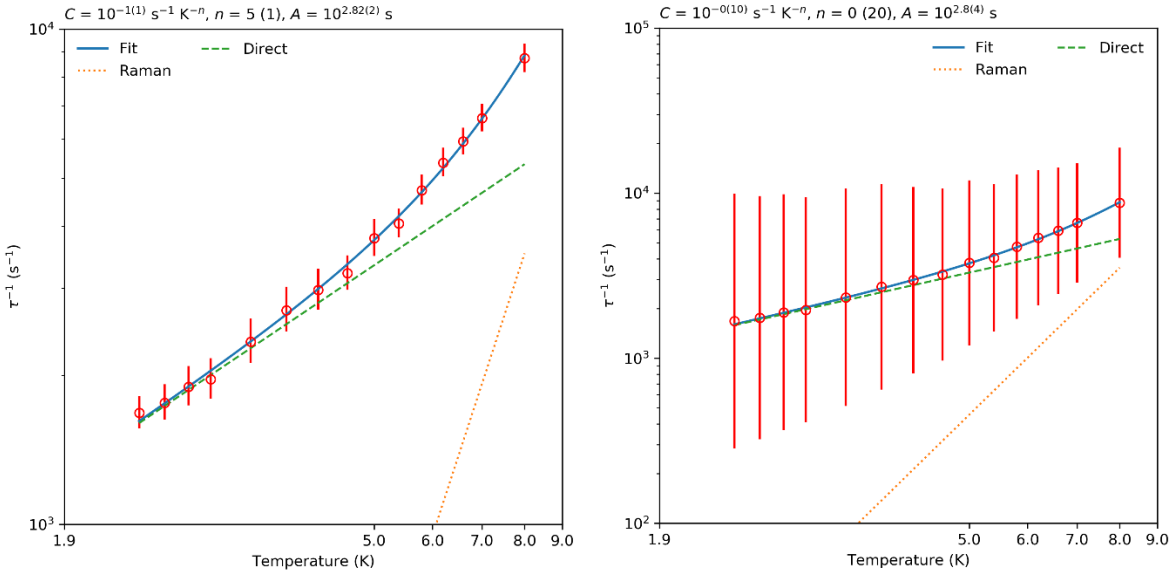

Figure S61: Log-log plots of τ^{-1} vs temperature for complex **5**, recorded at 2000 Oe applied field. Error bars represent either estimated error in fitting of τ from AC susceptibility data by generalised Debye model (left) or ESDs calculated from alpha parameter (right). Fit conducted and figure generated using the CC-FIT2 software package.[11]

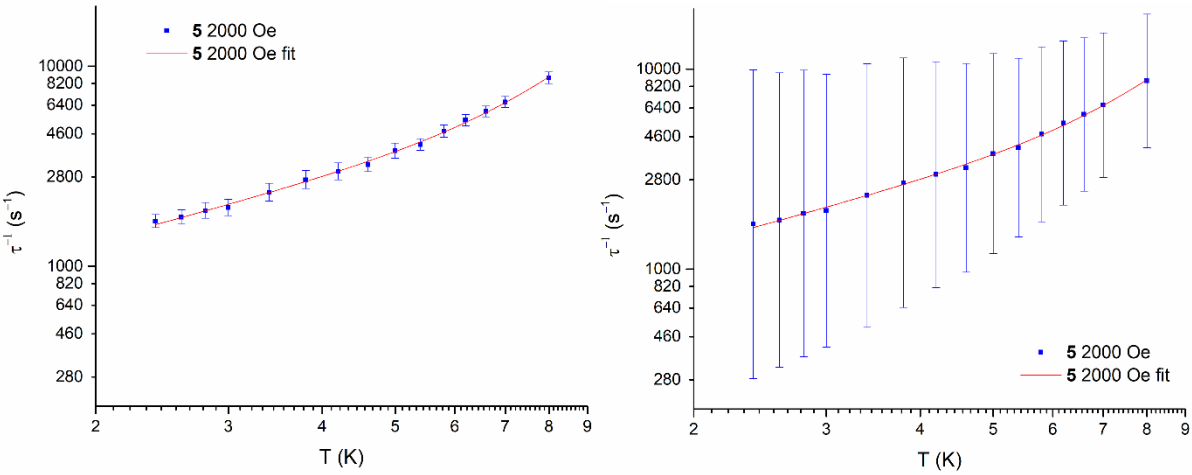

Figure S62: Replot of Figure S61, with identical y-axes for ease of comparison.

Table S16: Summary of AC magnetic data for **1**–**5**, calculated with consideration of ESDs derived from the alpha parameter. Parentheses indicate the error on the associated parameter.

Compound	H_{max} (Oe)	$\log_{10}[C/(s^{-1} K^{-n})]$	n	$\log_{10}[A/(s^{-1} K^{-1})]$
1	1000	-1.1(6)	4.9(7)	0.8(3)
2	1750	-1(2)	5(3)	2.1(3)
3	1000	-1(1)	5(1)	1.7(2)
4	2000	0(3)	5(4)	2.2(4)
5	2000	0(10)	0(20)	2.8(4)

S7.6.2 – Fitting to Wu relaxation model

$$\tau^{-1} = \frac{4\hbar\omega\Gamma|a|^2}{((\hbar\omega)^2\delta)^2 + (2\hbar\omega)^2} e^{-\hbar\omega/k_B T} + 10^A T$$

Equation S1: Expression for spin-phonon relaxation rate proposed by Wu,[13] plus direct term ($10^A T$). $\hbar\omega$ stands for the Raman active vibrational mode energy, Γ for the phonon linewidth, *a* for the spin-phonon coupling, and δ for the intra-Kramers doublet splitting. We fix $\boldsymbol{\Gamma}$ = 10 cm^{-1} and δ = 0.01 cm^{-1}, but the obtained simulations are not particularly sensitive to these parameters.

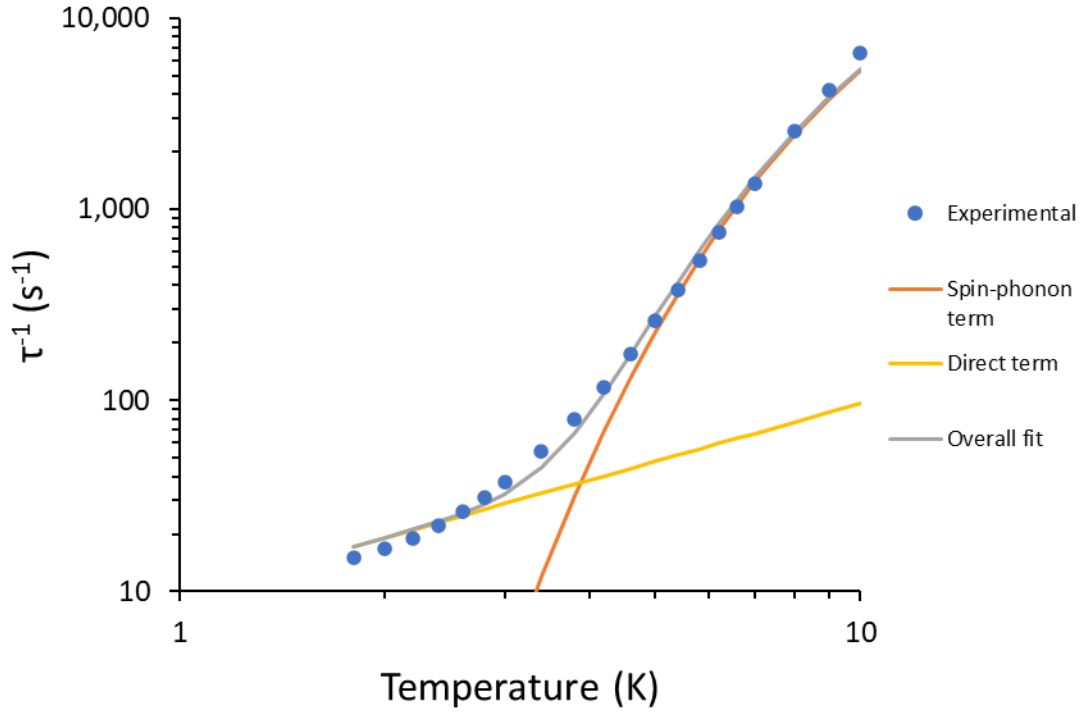

Figure S63: Relaxation profile for **1** with fitting according to Equation S1.

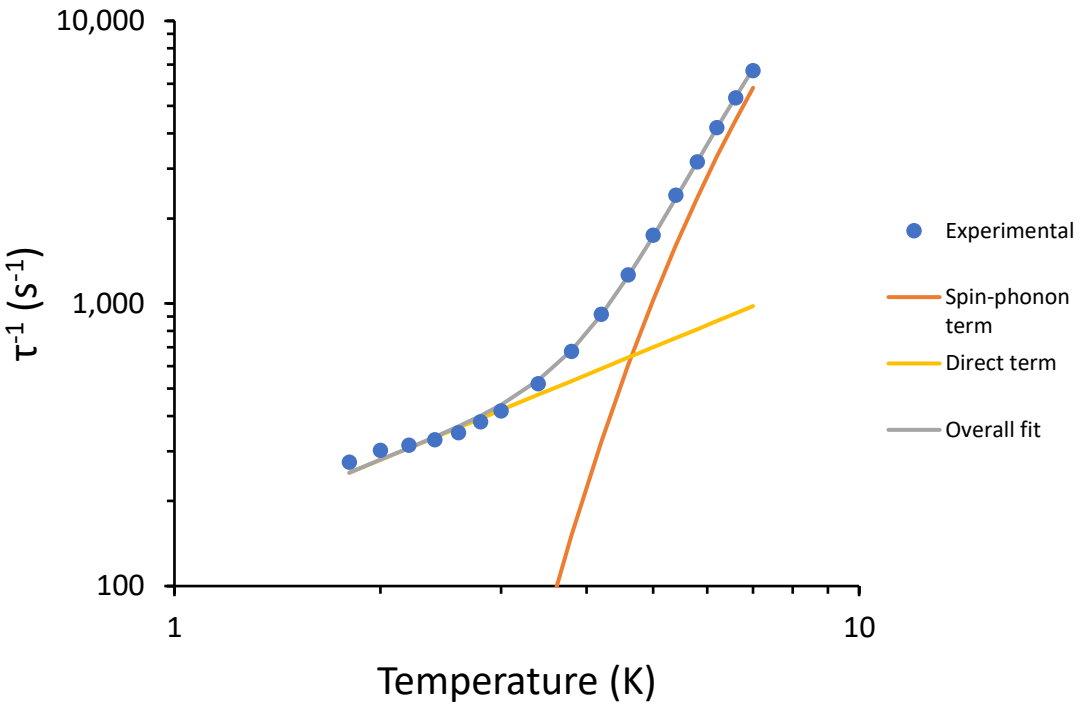

Figure S64: Relaxation profile for **2** with fitting according to Equation S1.

Table S17: Fitting parameters for **1** and **2** obtained by use of model in Equation S1.

Compound	a (cm^{-1})	$\hbar\omega$ (cm^{-1})	Γ (cm^{-1})	δ (cm^{-1})	A
1	6240	31.4	10	0.01	0.982
2	11500	30.3	10	0.01	2.15

S7.6.3 – Fitting to Lunghi relaxation model

$$\tau = \sum_{i=1,2} \frac{\hbar\omega_i}{V_{02}^i}\left[e^{\frac{\beta\hbar\omega_i}{2}} + \frac{(U_0 - \hbar\omega_i)^2}{(\hbar\omega_i)^2} e^{\frac{3}{2}\beta\hbar\omega_i}\right]$$

Equation S2: Expression for spin-phonon relaxation time proposed by Lunghi.[14] $\hbar\omega$ $\hbar\omega_i$stands for the energy of i^{th} phonon i, V_{02}^i for the *square* of the spin-phonon coupling associated to i^{th} phonon, β = $(1/k_BT)$,U_0 = excitation energy between electronic states.

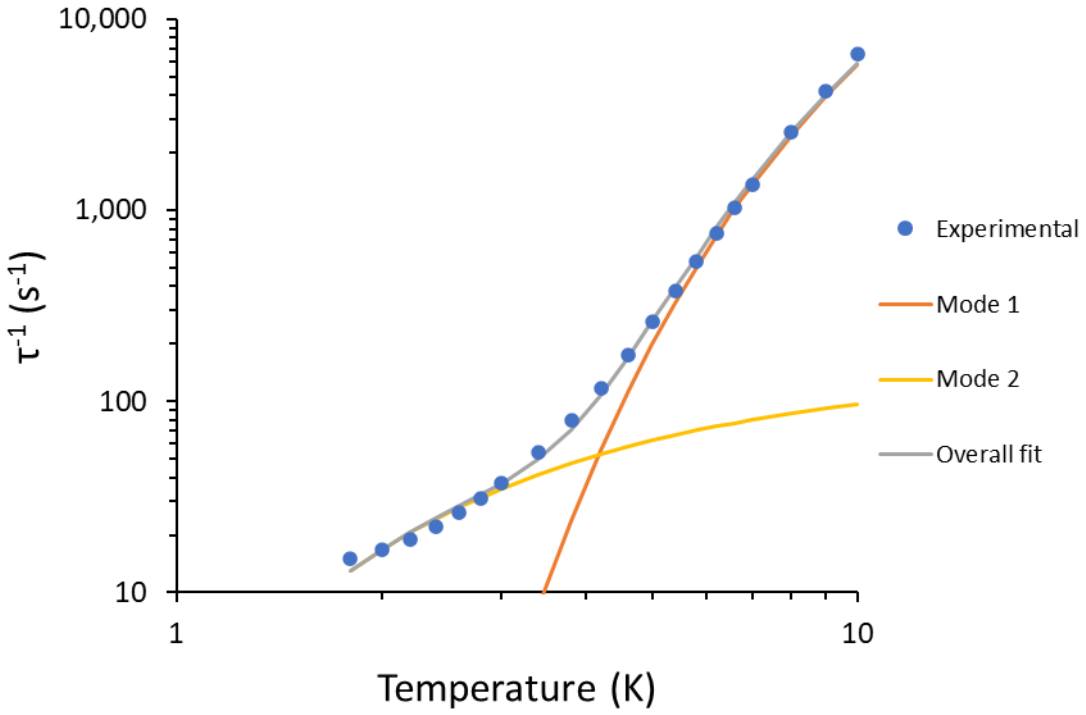

Figure S65: Relaxation profile of **1** with fitting to two vibrational phonon modes according to Equation S2.

Table S18: Fitting parameters for the two phonon modes of **1** obtained by use of model in Equation S2.

Phonon mode	$(V_{02})^{1/2}$ (cm^{-1})	$\hbar\omega$ (cm^{-1})	U_{02} (cm^{-1})
1	12900	22.5	0.1
2	54.8	3.06	0.1

S8 – References

1 A. J. Valentine, A. M. Geer, L. J. Taylor, A. M. Teale, K. E. Wood, H. E. L. Williams, W. Lewis, S. P. Argent, J. McMaster and D. L. Kays, *Dalton Trans.*, 2021, **50**, 722–728.

2 H. Y. Liu, B. Scharbert and R. H. Holm, *J. Am. Chem. Soc.*, 1991, **113**, 9529–9539.

3 G. W. A. Fowles, D. A. Rice and R. A. Walton, *J. Inorg. Nucl. Chem.*, 1969, **31**, 3119–3131.

4 H. R. Sharpe, A. M. Geer, L. J. Taylor, B. M. Gridley, T. J. Blundell, A. J. Blake, E. S. Davies, W. Lewis, J. McMaster, D. Robinson and D. L. Kays, *Nat. Commun.*, 2018, **9**, 3757.

5 C. Hansch, A. Leo and R. W. Taft, *Chem. Rev.*, 1991, **91**, 165–195.

6 *CrysAlisPRO*, Oxford Diffraction/Agilent Technologies UK Ltd, Yarnton, England.

7 G. M. Sheldrick, *Acta Crystallogr. Sect. A Found. Crystallogr.*, 2015, **71**, 3–8.

8 G. M. Sheldrick, *Acta Crystallogr. Sect. C Struct. Chem.*, 2015, **71**, 3–8.

9 O. V. Dolomanov, L. J. Bourhis, R. J. Gildea, J. A. K. Howard and H. Puschmann, *J. Appl. Crystallogr.*, 2009, **42**, 339–341.

10 G. A. Bain and J. F. Berry, *J. Chem. Educ.*, 2008, **85**, 532–536.

11 D. Reta and N. F. Chilton, *Phys. Chem. Chem. Phys.*, 2019, **21**, 23567–23575.

12 N. F. Chilton, R. P. Anderson, L. D. Turner, A. Soncini and K. S. Murray, *J. Comput. Chem.*, 2013, **34**, 1164–1175.

13 L. Gu and R. Wu, *Phys. Rev. Lett.*, 2020, **125**, 117203.

14 A. Lunghi, F. Totti, R. Sessoli and S. Sanvito, *Nat. Commun.*, 2017, **8**, 14620.

15 I. Fdez. Galván, M. Vacher, A. Alavi, C. Angeli, F. Aquilante, J. Autschbach, J. J. Bao, S. I. Bokarev, N. A. Bogdanov, R. K. Carlson, L. F. Chibotaru, J. Creutzberg, N. Dattani, M. G. Delcey, S. S. Dong, A. Dreuw, L. Freitag, L. M. Frutos, L. Gagliardi, F. Gendron, A. Giussani, L. González, G. Grell, M. Guo, C. E. Hoyer, M. Johansson, S. Keller, S. Knecht, G. Kovačević, E. Källman, G. Li Manni, M. Lundberg, Y. Ma, S. Mai, J. P. Malhado, P. Å. Malmqvist, P. Marquetand, S. A. Mewes, J. Norell, M. Olivucci, M. Oppel, Q. M. Phung, K. Pierloot, F. Plasser, M. Reiher, A. M. Sand, I. Schapiro, P. Sharma, C. J. Stein, L. K. Sørensen, D. G. Truhlar, M. Ugandi, L. Ungur, A. Valentini, S. Vancoillie, V. Veryazov, O. Weser, T. A. Wesołowski, P. O. Widmark, S. Wouters, A. Zech, J. P. Zobel and R. Lindh, *J. Chem. Theory Comput.*, 2019, **15**, 5925–5964.

16 B. O. Roos, R. Lindh, P. Å. Malmqvist, V. Veryazov and P. O. Widmark, *J. Phys. Chem. A*, 2004, **108**, 2851–2858.

17 B. O. Roos, R. Lindh, P. Å. Malmqvist, V. Veryazov and P. O. Widmark, *J. Phys. Chem. A*, 2005, **109**, 6575–6579.

18 L. Ungur and L. F. Chibotaru, *Chem. Eur. J.*, 2017, **23**, 3708–3718.

19 J. Finley, P. Å. Malmqvist, B. O. Roos and L. Serrano-Andrés, *Chem. Phys. Lett.*, 1998, **288**, 299–306.